Helical orbitals in electrical unidirectional molecular motors

Štěpán Marek [*]
Halle-Berlin-Regensburg Cluster of Excellence CCE, Universitttstraße 31, 93053 Regensburg, Germany;
Regensburg Center for Ultrafast Nanoscopy, University of Regensburg, Universitätstraße 31, 93053 Regensburg, Germany;
Institute of Theoretical Physics, University of Regensburg, Universitätstraße 31, 93053 Regensburg, Germany;
and Department of Condensed Matter Physics, Faculty of Mathematics and Physics, Charles University,
Ke Karlovu 5, 121 16 Praha 2, Czech Republic

Wulf Wulfhekel
Institute for Quantum Materials and Technologies, Karlsruhe Institute of Technology, 76021 Karlsruhe, Germany

Ferdinand Evers [†]
Institute of Theoretical Physics, University of Regensburg and Halle-Berlin-Regensburg Cluster of Excellence CCE,
Universitätstraße 31, 93053 Regensburg, Germany

Richard Korytár [‡]
Department of Condensed Matter Physics, Faculty of Mathematics and Physics,
Charles University, Ke Karlovu 5, 121 16 Praha 2, Czech Republic

(Received 20 October 2025; accepted 30 January 2026; published 10 March 2026)

The generation of unidirectional motion has been a long-standing challenge in engineering of molecular motors. Here, a mechanism driving the rotation is presented based on electron current through helical orbitals on a π-bonded carbon chain. Such electron current through helical orbitals has been shown to be circulating around the carbon chain. It is natural to expect that the associated electronic angular momentum drives a rotation when the current is turned on. As intuitive as this relation might seem, it is also incomplete because a formal definition of helicality in terms of a physical observable has not yet been given. Such a definition is proposed here. Based on this definition, we show how helicality determines the motor's sense of rotation. We exemplify the relation between helicality and angular momentum in Hückel models of linear carbon chains (cumulenes and oligoynes). We attribute the previously reported opposite helicality sense of frontier orbitals (highest occupied molecular orbital and lowest unoccupied molecular orbital) to the approximate sublattice symmetry. For oligoynes, this symmetry is hidden in the sense that it does not reduce to a mere labeling of atoms. Sublattice symmetry, combined with time-reversal invariance, allows us to derive Onsager-type reciprocal relations of various linear response coefficients, dictating, e.g., an odd energy dependence of angular momentum response to voltage bias. We propose an observable consequence of the approximate sublattice symmetry: If the carbon chain is employed as an axle of a molecular rotor, the sense of rotation is independent on the direction of the current.

DOI: 10.1103/zx3k-hkph

I. INTRODUCTION

Molecular motors are molecules that can perform controlled and directed rotational motion, powered by light, an electrochemical environment or a chemical reaction [1–4]. The rotational mechanism usually results from the following simplified picture: The rotational angle θ (a slow degree of freedom) is constrained to an equilibrium value θ_0 by a potential, $V_0(\theta)$, hindering the rotation. The excitation induces a fast change of the potential to $V_1(\theta)$, followed by a relaxation to a different equilibrium, θ_1. The directionality emerges because one of these potentials is not symmetric with regard to clockwise or anticlockwise rotation sense (a "ratchet") [5,6].

In recent years, the tip of a scanning-tunneling microscope has been used to wire molecules into a circuit and drive their rotation by the electric current, $I(t)$ [7–17]. For example, it was reported that $I(t)$ switches in time through three fixed levels I_A, I_B, I_C such that the sequence ABC occurs much more often than ACB [10,18,19]. This switching was attributed to a directional rotation (as opposed to a stochastic motion) and corroborated by scanning-tunneling maps [10]. The current-induced rotation has been usually described in terms of inelastic electron-vibrational transitions [20,21] or electronic current-induced wind-forces [21–24]. Until now, such descriptions have not invoked a specific orbital topology.

[*]Contact author: stepan.marek@physik.uni-regensburg.de
[†]Contact author: ferdinand.evers@physik.uni-regensburg.de
[‡]Contact author: richard.korytar@physik.uni-regensburg.de

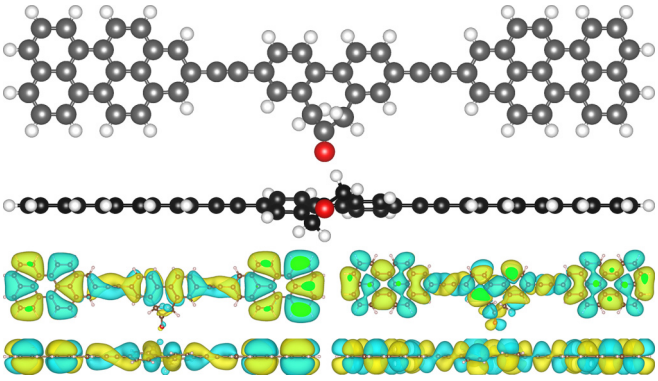

FIG. 1. Top: Atomic structure of a molecular motor, containing a central rotating moiety and left and right stators (C = gray, H = white, O = red). The pair of connecting –C ≡ C– chains are molecular axles and bearings. The rotor's hexagonal rings are tilted by ≈29°, because of the oxygen bridge. Each axle is attached to two hexagons that can be tilted with respect to each other, giving rise to helical orbitals. Bottom: isosurface of the highest occupied molecular orbital (left) and the lowest occupied molecular orbital (right) calculated in DFT, showing helical orbitals along the axles with opposite winding senses. The bottom row portrays these orbitals from a side view.

Here, we explore a driving force that utilizes directly the angular momentum and helicity of electrons transported along the motor's axle. Recently, this concept has been explored on the classical level by Korytár and Evers [25]. The authors used a model with a particle moving along a narrow helical tube. The current of such particles gave rise to a directed rotation of the tube due to angular momentum conservation. In this work we extend this idea to the quantum-mechanical world. We show that helical orbitals on a π-bonded carbon chain can act analogously to a helical trajectory.

Helical orbitals naturally reside in many π-bonded carbon chains [26]. The simplest examples are cumulenes with end groups that lower the chain symmetry down to C_2 or C_1 (axial chirality). When these chains bridge a molecular junction with a voltage bias, the electric current winds around the chain in a helical fashion, as shown by Garner *et al.* [27]. Inspired by Skolaut [18], we employ the linear carbon chain as an axle connecting rotor and stator moieties of a molecular motor. Figure 1 portrays a sample structure and its frontier orbitals. We argue that the steady-state current flowing through such a molecular architecture is accompanied by a finite expectation value of electronic angular momentum with respect to the axle. We demonstrate this by evaluating both helicality and angular momentum of carbon chains in nonequilibrium.

To this end, we employ a Hückel model [28] of the π orbitals of the carbon chain. The model is applicable both to cumulenes (carbon chains with consecutive double bonds) and oligoynes (alternating single and triple bond). Hückel modeling was proven to exhibit all essential features of helical orbitals as shown by Garner *et al.* by comparing with *ab initio* calculations [29]. Helicality of an orbital can be quite generally quantified as an average angle of turning of the π orbital over one C–C bond. In this spirit, helicality has been evaluated for particular Hückel or *ab initio* wavefunctions [29,30]. We go beyond these works by introducing a Hermitian operator $\hat{h}$. The sign of the expectation value $\langle\psi|\hat{h}|\psi\rangle$ determines the clockwise or anticlockwise winding sense of an orbital $|\psi\rangle$. For weakly varying wavefunctions, the $\hat{h}$ delivers an average sine of the twisting angle directly.

Promoting helicality to an operator $\hat{h}$ is advantageous for several reasons: (1) Formally, helicality becomes an observable. (2) Helicality can be evaluated not only for isolated chains but also for embedded chains attached to electrodes (molecular junctions), in nonequilibrium. (3) In the continuum limit, helicality adopts a transparent form, $\hat{h} \propto \hat{l}\hat{p}$, where $\hat{l}$ is orbital angular momentum of transverse motion and $\hat{p}$ is linear momentum along the chain. The operator product $\hat{l}\hat{p}$ is a *helicity* of a quasi one-dimensional motion. Helicity, in kinematics, is a quantity defined as the projection of the angular momentum to the direction of motion. Replacing the orbital $\hat{l}$ by the spin component, helicity plays an essential role as an invariant of free Dirac fermions. Electronic helicity (termed chirality if excitations are gapless) appears as a conserved quantity in edge states of quantum spin-Hall devices [31], in Weyl semimetals [32] and it has been proposed to generate spin currents in helical molecular junctions [33,34]. Our result therefore clarifies a connection between helicality, understood as a winding of molecular orbitals and helicity (chirality). Functional applications of electronic chirality in quantum materials are being actively researched [35,36].

We demonstrate that both types of carbon chains—cumulenes and oligoynes—are endowed with a sublattice (SL) symmetry. The latter plays an important role in bipartite lattices. For example, planar sp^2-hybridized carbon graphenoid structures (ribbons, flakes, etc.) encompass two triangular sublattices [37]. When the electronic structure of such systems is modeled by nearest-neighbor tight-binding Hamiltonians, the salient eigenenergies arrange symmetrically around the band center (see reviews [38–40]). In theoretical chemistry, this is known as the Coulson-Rushbrooke theorem [41,42]. The operator $\hat{P}$ that maps an eigenstate to its mirror partner (in energy space) merely assigns a minus sign to the wavefunction values on one of the sublattices. Unlike standard symmetries [43,44], which are expressed by commutation with the Hamiltonian $\hat{H}$, the SL symmetry is formulated by an anticommutator: $\hat{H}\hat{P} + \hat{P}\hat{H} = 0$. Consequently, there is no conserved quantity, but a symmetry of eigenenergies and respective eigenvectors. Perhaps the earliest occurrence of this "nonstandard" symmetry in quantum physics was the mass-less limit of the Dirac equation [45]. In such contexts, the symmetry is called *chiral* [46], but this label should not be confused with structural chirality.

The presence of SL symmetry in *sp*-hybridized carbon chains is less obvious for two reasons: First, unlike in planar sp^2 hybridized carbon matter, there are two p orbitals per carbon in the π system of the chain. Second, the chains are terminated by end groups (e.g., methyl, H, H_2) that have a decisive role in the formation of helical eigenstates. We show that cumulenes have a bipartite lattice that has a rather familiar form: labeling carbons based on their parity along the chain. In the case of oligoynes, the SL symmetry is not apparent from the Hamiltonian matrix; we say that it is hidden. As we show, SL symmetry enforces opposite helicality between each molecular orbital and its SL mirror partner.

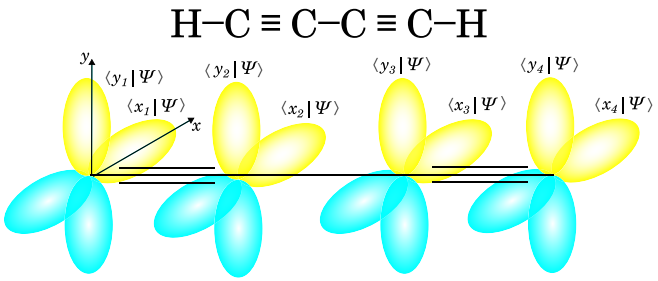

FIG. 2. Top: Diacetylene (butadiyne), a member of the oligoyne family with four carbons. Bottom: The Hückel wavefunction of the π orbitals is represented in the basis of $p_{x,y}$ orbitals on each carbon.

We employ nonequilibrium Green's function method to evaluate observables of the chain coupled to leads with bias voltage. The SL symmetry imposes certain conditions on linear response functions of helicality and angular momentum. These newly derived relations belong to Onsager reciprocities since they involve an operation of time reversal (microreversibility). Most importantly, the response coefficient of angular momentum (with respect to small bias) is antisymmetric with respect to the chain's band center.

We find that the expectation value of angular momentum essentially mirrors the behavior of the orbital winding when the level broadening is larger than the molecular level spacing. Finally, we discuss the implications of the angular momentum hosted by helical orbitals for molecular motors and rotors.

II. MODEL HAMILTONIAN AND OBSERVABLES

The model in which we study the relation of helicality and angular momentum is described in this section. We introduce the Hamiltonian and define the respective observables: the angular momentum and helicality operators. We also describe the coupling to the leads and finally show that the helicality operator attains a transparent form in the continuum limit.

A. Model

We employ a Hückel (tight-binding) model to represent linear chains of *sp*-hybridized carbon atoms. We start with the simpler case of C chains with hydrogens as end groups. To induce helical eigenstates, we introduce some more complicated end groups in Sec. II A 2, describing methyl-terminated oligoynes and cumulenes.

1. Hamiltonian of H-terminated oligoynes

First, we start with the Hamiltonian of oligoynes: *sp*-hybridized carbon chains with H– end groups (see Fig. 2). The basis set of the tight-binding model contains a p_x and a p_y state on each carbon; z is the chain axis. The basis is labeled and ordered as follows:

$$(|x_1\rangle \quad |y_1\rangle \quad |x_2\rangle \quad |y_2\rangle \quad \cdots), \tag{1}$$

where $|x/y_n\rangle$ stands for the $p_{x/y}$-orbital on the nth carbon, respectively. The Hamiltonian of a chain with N carbons has a transparent bra-ket form

$$\hat{H}_0 := -t \sum_{n=1,3,\ldots}^{N} [|x_n\rangle\langle x_{n+1}| + |y_n\rangle\langle y_{n+1}| + \text{H.c.}] \tag{2}$$

$$- t' \sum_{n=2,4,\ldots}^{N} [|x_n\rangle\langle x_{n+1}| + |y_n\rangle\langle y_{n+1}| + \text{H.c.}], \tag{3}$$

where $-t$ and $-t'$ are the tunneling matrix elements (resonance integrals or hopping elements) and H.c. stands for Hermitian conjugate. The difference in t and t' is due to dimerization: In the above equation, $-t$ pertains to bonds 1–2, 3–4, … and $-t'$ to 2–3, 4–5, etc. The on-site energy has been put to zero.

Because of symmetry, the p_x states do not couple to the p_y states. As a consequence, $\hat{H}_0$ is a direct sum of two identical nearest-neighbor coupled chains. The eigenstates are not helical, because the system owns a C_∞ axis of rotation.

It will be useful to represent some operators as direct products. The basis can be relabeled as $(|\alpha, n\rangle)$ with the site index n and $\alpha = \pm 1$ for $p_{x/y}$. In the case $t = t'$, which will be discussed from Sec. II B onwards, the matrix elements $\langle \alpha, n|H_0|\alpha', n'\rangle$ can be represented as

$$-t(\mathbb{T} + \mathbb{T}^\top) \otimes \hat{\sigma}_0. \tag{4}$$

The matrix $\mathbb{T}$ adopts the indices n, n' and $\hat{\sigma}_0$, the 2×2 identity matrix, and the indices α, α'. The $N \times N$ matrix $\mathbb{T}$ is given by

$$\mathbb{T} := \begin{pmatrix} 0 & 1 & 0 & \ldots & 0 \\ 0 & 0 & 1 & \ddots & \vdots \\ & & \ddots & \ddots & 0 \\ & & & \ddots & 1 \\ & & & & 0 \end{pmatrix}. \tag{5}$$

2. Effect of end groups in cumulenes and oligoynes

To lower the chain symmetry, we consider here replacing the H– groups by, e.g., a methyl H_3C– or a hydrogen pair, H_2– (see Fig. 3). We assume that the group consists of sigma bonds only, which are decoupled from the π system of the C chain and well energetically separated from it, so that these states can be truncated. The Hamiltonian of a carbon chain with such groups can be written as

$$\hat{H} := \hat{H}_0 + \hat{H}_1 + \hat{H}_N, \tag{6a}$$

$$\hat{H}_1 := \sum_{\alpha,\alpha'} h^{(1)}_{\alpha,\alpha'} |1, \alpha\rangle\langle 1, \alpha'|, \tag{6b}$$

$$\hat{H}_N := \sum_{\alpha,\alpha'} h^{(N)}_{\alpha,\alpha'} |N, \alpha\rangle\langle N, \alpha'|, \tag{6c}$$

with $\hat{H}_0$ from Eq. (3) and the Hermitian matrices $\hat{h}^{(1,N)}$ representing the end groups and the consecutive loss of the C_∞ symmetry on the sites 1 and N.

Having in mind applications of carbon chains as bridges in molecular junctions, and, most importantly, as axles in molecular motors, we consider two end groups rotated with respect to each other by a dihedral angle θ_T. This motivates us to relate the end group terms by

$$\hat{h}^{(N)} = \hat{R}(\theta_T)\hat{h}^{(1)}\hat{R}(-\theta_T), \tag{7a}$$

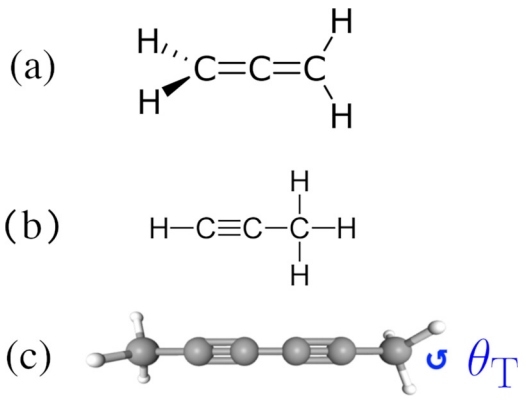

FIG. 3. Examples of carbon chains with different end groups. (a) Propadiene with sp^2 hybridized end carbons, belongs to allenes. Longer variants, with additional double-bonded carbons inserted in the chain, are called cumulenes. (b) Propyne can be seen as an oligoyne with a substituted methyl group. (c) 2,4-hexadiyne with two methyl end groups, belongs to oligoynes. We treat the relative angle θ_T of the two groups as a parameter. In cumulenes and allenes, carbons are double bonded. Single and triple bonds alternate in oligoynes.

where the rotation matrix is

$$\hat{R}(\theta_T) = \begin{pmatrix} \cos(\theta_T) & -\sin(\theta_T) \\ \sin(\theta_T) & \cos(\theta_T) \end{pmatrix} \tag{7b}$$

and matrix product was employed.

The Hamiltonian (6) captures distinct types of end groups. In this work, we focus on two types of end groups:

Model 1—cumulenes. For example, propadiene [Fig. 3(a)]. Here, the end carbons are sp^2 hybridized ($N = 3$). Thus, one of the $p_{x,y}$ orbitals at the end carbons drops out from the Hilbert's space (1). This can be achieved by the matrix

$$\hat{h}^{(1)} = \begin{pmatrix} \epsilon & 0 \\ 0 & 0 \end{pmatrix}, \text{ and taking } \epsilon \to \infty. \tag{8}$$

Here, $\theta_T = \frac{\pi}{2}$. For $N > 3$ these compounds belong to cumulenes. The Hamiltonian with the matrices (8,7) is equivalent to the Hamiltonians investigated thoroughly in Refs. [29,47]. We revisit this model because our analytical framework allows to rationalize and explain some numerical results presented in those earlier works.

Model 2—oligoynes. This model captures chains with each end group of the H_3C– type, as, e.g., in propyne in Fig. 3(b) or in 2,4-hexadiyne in Fig. 3(c). The carbons of the H_3C– groups are sp^3 hybridized. Their effect on the neighboring carbon sites is accounted for by the Hermitian matrices $\hat{h}^{(1,N)}$, small in magnitude in comparison to t. For general θ_T, helical eigenstates can be expected due to axial chirality [26]. To investigate qualitatively the occurrence of helicality with such boundary terms, we simplify the matrix $\hat{h}^{(1)}$ to the Ansatz

$$\hat{h}^{(1)} = \begin{pmatrix} 0 & 0 \\ 0 & \epsilon \end{pmatrix}, \tag{9}$$

with $0 < |\epsilon| \ll t$. With this parametrization, the matrix commutator $[\hat{h}^{(1)}, \hat{h}^{(N)}]$ is nonvanishing, except for $\theta_T = 0, \pm\frac{\pi}{2}, \pm\pi, \ldots$, which implies a certain point symmetry.

Most of this work employs Model 2, and Model 1 (distinguishing itself by a large ϵ) is invoked only when stated explicitly. In both cases, it will be advantageous to express the end-group terms in a general form

$$\hat{h}^{(1)} = a^{(1)}\hat{\sigma}_0 + b^{(1)}\hat{\sigma}_1 + c^{(1)}\hat{\sigma}_3, \tag{10a}$$

$$\hat{h}^{(N)} = a^{(N)}\hat{\sigma}_0 + b^{(N)}\hat{\sigma}_1 + c^{(N)}\hat{\sigma}_3. \tag{10b}$$

We note that the $\hat{\sigma}_2$ term is absent due to time-reversal invariance and the $\hat{\sigma}_0$ terms do not select any spatial direction. Using the $N \times N$ matrices (projectors on the end carbons)

$$\mathbb{B}_1 := \begin{pmatrix} 1 & 0 & \cdots \\ 0 & 0 & \cdots \\ \vdots & \vdots & \ddots \end{pmatrix}, \quad \mathbb{B}_N := \begin{pmatrix} \ddots & \vdots & \vdots \\ \cdots & 0 & 0 \\ \cdots & 0 & 1 \end{pmatrix}, \tag{11}$$

the end-group terms in Eq. (6) can written in a product form

$$\hat{H}_1 = \mathbb{B}_1 \otimes \hat{h}^{(1)}, \tag{12a}$$

$$\hat{H}_N = \mathbb{B}_N \otimes \hat{h}^{(N)}. \tag{12b}$$

3. Coupling to the leads

To carry our calculation over to the nonequilibrium caused by coupling to the leads and the voltage drop, we introduce the self-energy $\hat{\Sigma}(E) = \hat{\Sigma}_L(E) + \hat{\Sigma}_R(E)$. Our analytical results are pursued with only minimal symmetry-imposed constraints on the form of $\hat{\Sigma}(E)$, to be specified later.

When chains are bridged across a molecular junction, the left and right leads couple to the chain's respective end, i.e., site 1 and site N. For our numerical analysis, we adopt a simplified coupling model, represented by self-energy matrices

$$\hat{\Sigma}_L = -i\eta\mathbb{B}_1 \otimes \hat{\sigma}_0, \tag{13a}$$

$$\hat{\Sigma}_R = -i\eta\mathbb{B}_N \otimes \hat{\sigma}_0, \tag{13b}$$

where Eq. (11) has been used. This model assumes that both p orbitals at the end carbons couple equally to the leads (cylindrical symmetry) with absorption rate η ("wide band").

The left and right boundary is coupled to reservoirs with zero-temperature Fermi distributions $f_{L/R}(E) = \Theta(\mu_{L/R} - E)$ and respective chemical potentials $\mu_{L/R}$. The difference $\mu_L - \mu_R = eV$ is the external voltage bias.

B. Observables

In this section, we formulate expressions for the angular momentum, electric current, and helicality operators within the Hückel model described previously. We explain the calculation of their expectation values in nonequilibium, present some commutaion relations, and perform the continuum limit of the helicality operator.

1. Recap: Green's function formalism

Green's functions. Before we formulate the relevant operators, we digress to recall the technique for the evaluation of observables in presence of two reservoirs (following Refs. [48,49]). It is advantageous to express expectation values of operators using nonequilibrium Green's functions [50]. For a one-body operator $\hat{O}$ (matrix elements $\langle n\alpha|\hat{O}|n'\alpha'\rangle$), its expectation is given by

$$O(E_F, V) := \langle\hat{O}\rangle_{E_F,V} = -i\int \frac{dE}{2\pi}\mathrm{Tr}[\hat{O}\hat{G}^<(E)], \tag{14}$$

where $\hat{G}^<(E)$ denotes the lesser Green's function

$$\hat{G}^<(E) = \mathrm{i}\hat{G}^{(\mathrm{R})}(E)[\hat{\Gamma}_\mathrm{L}(E)f_\mathrm{L}(E) + \hat{\Gamma}_\mathrm{R}(E)f_\mathrm{R}(E)]\hat{G}^{(\mathrm{A})}(E). \tag{15}$$

Matrix multiplication is implied. The advanced (A) and retarded (R) Green's functions are defined by

$$\hat{G}^{(\mathrm{R})}(E) \coloneqq [E\hat{1} - \hat{H} - \hat{\Sigma}(E)]^{-1}, \tag{16}$$

$$\hat{G}^{(\mathrm{A})}(E) \coloneqq [\hat{G}^{(\mathrm{R})}(E)]^\dagger. \tag{17}$$

We note that in the above expressions, the quantities with hats should be understood as matrices; likewise $\hat{1}$ is a unit matrix. Finally, the definitions

$$\hat{\Gamma}_{\mathrm{L,R}}(E) = -\mathrm{i}(\hat{\Sigma}^\dagger_{\mathrm{L,R}}(E) - \hat{\Sigma}_{\mathrm{L,R}}(E))$$
$$\hat{\Gamma}(E) = -\mathrm{i}(\hat{\Sigma}^\dagger(E) - \hat{\Sigma}(E))$$

complete the recapitulation of Green's function formulas.

Equilibrium and linear response. Equation (15) can be reshaped to contain expressions symmetric and antisymmetric in the Fermi functions,

$$\hat{G}^<(E) = \frac{\mathrm{i}}{2}\hat{G}^{(\mathrm{R})}(E)[\hat{\Gamma}_\mathrm{L}(E) + \hat{\Gamma}_\mathrm{R}(E)]\hat{G}^{(\mathrm{A})}(E) \tag{18a}$$
$$\times [f_\mathrm{L}(E) + f_\mathrm{R}(E)] \tag{18b}$$
$$+ \frac{\mathrm{i}}{2}\hat{G}^{(\mathrm{R})}(E)[\hat{\Gamma}_\mathrm{L}(E) - \hat{\Gamma}_\mathrm{R}(E)]\hat{G}^{(\mathrm{A})}(E) \tag{18c}$$
$$\cdot [f_\mathrm{L}(E) - f_\mathrm{R}(E)]. \tag{18d}$$

In equilibrium, the odd term above vanishes, since $f_{\mathrm{L,R}}(E) = \Theta(E_\mathrm{F} - E)$. Hence,

$$O(E_\mathrm{F}, 0) = \int_{-\infty}^{E_\mathrm{F}} \mathrm{Tr}[\hat{O}\hat{A}(E)]\mathrm{d}E, \tag{19}$$

where we used Eq. (14) and defined the operator

$$\hat{A}(E) \coloneqq \frac{\mathrm{i}}{2\pi}[\hat{G}^{(\mathrm{R})}(E) - \hat{G}^{(\mathrm{A})}(E)] \tag{20a}$$
$$= \frac{1}{2\pi}\hat{G}^{(\mathrm{R})}(E)[\hat{\Gamma}_\mathrm{L}(E) + \hat{\Gamma}_\mathrm{R}(E)]\hat{G}^{(\mathrm{A})}(E), \tag{20b}$$

whose the diagonal elements are the familiar projected densities of states.

Certain observables vanish in thermodynamic equilibrium on symmetry grounds. We show in Sec. III A 3 that this is the case of angular momentum, for example. Vanishing of $O(E_\mathrm{F}, 0)$ requires $\mathrm{Tr}[\hat{O}\hat{A}(E)] = 0$ for all energies. For such observables, the trace in Eq. (14) is determined only by the odd term in Eq. (18). Explicitly,

$$O(E_\mathrm{F}, V) = \frac{1}{2}\int \mathrm{Tr}\{\hat{O}\hat{G}^{(\mathrm{R})}(E)[\hat{\Gamma}_\mathrm{L}(E) - \hat{\Gamma}_\mathrm{R}(E)]\hat{G}^{(\mathrm{A})}(E)\}[f_\mathrm{L}(E) - f_\mathrm{R}(E)]\frac{\mathrm{d}E}{2\pi}. \tag{21}$$

Expanding the Fermi functions in voltage

$$O(E_\mathrm{F}, V) = \frac{eV}{2}\int \mathrm{Tr}\{\hat{O}\hat{G}^{(\mathrm{R})}(E)[\hat{\Gamma}_\mathrm{L}(E) - \hat{\Gamma}_\mathrm{R}(E)]\hat{G}^{(\mathrm{A})}(E)\}\delta(E - E_\mathrm{F})\frac{\mathrm{d}E}{2\pi} + \mathcal{O}(V^2)$$

yields the linear-response coefficient

$$\left.\frac{\partial O(E_\mathrm{F}, V)}{\partial V}\right|_{V=0} = \frac{e}{4\pi}\mathrm{Tr}\{\hat{O}\hat{G}^{(\mathrm{R})}(E_\mathrm{F})[\hat{\Gamma}_\mathrm{L}(E) - \hat{\Gamma}_\mathrm{R}(E)]\hat{G}^{(\mathrm{A})}(E_\mathrm{F})\}. \tag{22}$$

2. Electric current

The electric current follows from a standard expression [49]

$$I(V) = \frac{2e}{h}\int \mathfrak{T}(E)[f_\mathrm{L}(E) - f_\mathrm{R}(E)]\mathrm{d}E, \tag{23}$$

with the transmission function

$$\mathfrak{T}(E) \coloneqq \mathrm{Tr}[\hat{G}^{(\mathrm{R})}(E)\hat{\Gamma}_\mathrm{L}(E)\hat{G}^{(\mathrm{A})}(E)\hat{\Gamma}_\mathrm{R}(E)]. \tag{24}$$

Expanding Eq. (23) to linear order in V yields a well-known Landauer formula for the differential conductance at $V = 0$,

$$\left.\frac{\mathrm{d}I}{\mathrm{d}V}\right|_{V=0} = \frac{2e^2}{h}\mathfrak{T}(E_\mathrm{F}).$$

3. Angular momentum

In the $\mathrm{p}_{x,y}$ basis, the z projection of the angular momentum satisfies the relations

$$\hat{L}_z|x_n\rangle = \mathrm{i}\hbar|y_n\rangle,$$
$$\hat{L}_z|y_n\rangle = -\mathrm{i}\hbar|x_n\rangle. \tag{25}$$

It can be seen that

$$\langle n, \alpha|\hat{L}_z|n', \alpha'\rangle = \hbar\,\delta_{nn'}(\hat{\sigma}_2)_{\alpha\alpha'},$$

with the Pauli matrix $\hat{\sigma}_2$. In the tensor-product notation of Eq. (4), the matrix elements of $\hat{L}_z$ read

$$\hat{L}_z = \hbar\mathbb{I} \otimes \hat{\sigma}_2, \tag{26}$$

where $\mathbb{I}$ is the $N \times N$ identity matrix.

The expectation value of $\hat{L}_z$ in presence of the reservoirs can be expanded in voltage

$$L_z(E_\mathrm{F}, V) \coloneqq \langle\hat{L}_z\rangle_{E_\mathrm{F},V} = L_z(E_\mathrm{F}, 0) + \frac{\partial L_z}{\partial V}(E_\mathrm{F}, 0)V + \mathcal{O}(V^2),$$

where the equilibrium term vanishes due to time-reversal invariance (to be proven in Sec. III A 3). Hence, Eq. (22) applies and delivers the linear-response coefficient of angular momentum,

$$\left.\frac{\partial L_z(E_\mathrm{F}, V)}{\partial V}\right|_{V=0} = \frac{e}{4\pi}\mathrm{Tr}\{\hat{L}_z\hat{G}^{(\mathrm{R})}(E_\mathrm{F})[\hat{\Gamma}_\mathrm{L}(E_\mathrm{F}) - \hat{\Gamma}_\mathrm{R}(E_\mathrm{F})]\hat{G}^{(\mathrm{A})}(E_\mathrm{F})\}. \tag{27}$$

4. Helicality operator

The most natural way to quantify helicality of an orbital is to measure its average winding angle per C–C bond. This idea was used to quantify helicality of wavefunctions previously [29,30]. Here, we extend this idea by formulating a Hermitian operator, whose expectation values quantify the winding of the molecular orbital.

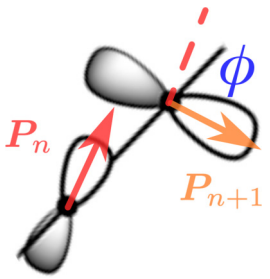

FIG. 4. Illustration of the helicality operator. A wavefunction on a given site n is a linear combination of p_x and p_y orbitals. Therefore, it is a p-orbital oriented along a unit vector $\boldsymbol{P}_n$. On the consecutive site, the unit vector $\boldsymbol{P}_{n+1}$ is tilted by an angle ϕ with respect to $\boldsymbol{P}_n$. The sign of ϕ determines the helicality of the given bond, i.e., the clockwise ($\phi > 0$) or anticlockwise winding of the π orbital along the bond with increasing n. Assuming $|\phi| < \pi$, the bond helicality is given by the sign of $\boldsymbol{e}_z \cdot (\boldsymbol{P}_n \times \boldsymbol{P}_{n+1}) = |\boldsymbol{P}_n||\boldsymbol{P}_{n+1}| \sin\phi$, where $\times$ is the cross-product. For a given wavefunction, we evaluate $\boldsymbol{P}_n \times \boldsymbol{P}_{n+1}$ as an expectation value of the local pitch density operator $\hat{h}_n$ introduced in Eq. (30).

A real wavefunction $\langle \alpha, n|\psi\rangle$ [living in the space spanned by Eq. (1)] can be represented geometrically by a series of N two-dimensional vectors,

$$\boldsymbol{P}_n := \begin{pmatrix} \langle x_n|\psi\rangle \\ \langle y_n|\psi\rangle \end{pmatrix}, \quad n = 1, \ldots, N,$$

pointing perpendicularly to the chain axis (z axis). The twisting of the orbital is measured by the relative angle of a bond pair $(\boldsymbol{P}_n, \boldsymbol{P}_{n+1})$. Vector algebra offers two ways to extract the angle: a scalar product and a vector product (or dot and cross products). Garner *et al.* explored the first option [29]. Here, we take the second one; we have

$$\boldsymbol{P}_n \times \boldsymbol{P}_{n+1} = \boldsymbol{e}_z\, |\boldsymbol{P}_n||\boldsymbol{P}_{n+1}| \sin(\phi)$$

or

$$\tilde{h}_n := \boldsymbol{e}_z \cdot (\boldsymbol{P}_n \times \boldsymbol{P}_{n+1}) = |\boldsymbol{P}_n||\boldsymbol{P}_{n+1}| \sin(\phi), \tag{28}$$

where the angle ϕ is the relative rotation (see Fig. 4). The advantage of (28) is that $\tilde{h}_n$ distinguishes between clockwise and anticlockwise evolution of vectors. This feature allows us to establish a relation between helicality, defined here, and angular momentum, in the next section.

With the definition of the $\times$ product, Eq. (28) turns into

$$\tilde{h}_n = \tfrac{1}{2}(\langle x_n|\psi\rangle^* \langle y_{n+1}|\psi\rangle - \langle y_n|\psi\rangle^* \langle x_{n+1}|\psi\rangle + \text{c.c.}), \tag{29}$$

where we symmetrized the formula to generalize for complex wavefunctions (c.c. is complex conjugate). Equation (29) can be understood as an expectation value of a bond operator

$$\hat{h}_n = \tfrac{1}{2}(|x_n\rangle\langle y_{n+1}| - |y_n\rangle\langle x_{n+1}| + \text{H.c.}). \tag{30}$$

We define the helicality operator by the expression

$$\hat{h} = \frac{1}{2} \sum_{n=1}^{N-1} (|x_n\rangle\langle y_{n+1}| - |y_n\rangle\langle x_{n+1}| + \text{H.c.}). \tag{31}$$

Its expectation values convey the average of the vector products (28) over all bonds. For $|\psi\rangle$ that is varying homogeneously along the chain, $|\boldsymbol{P}_n| \approx 1/\sqrt{N}$. It can be shown that for long chains $\langle\psi|\hat{h}|\psi\rangle$ offers a straightforward interpretation as an average sine of the consecutive p-orbitals' turning angle (see Appendix A 1). In Appendix A 2, we evaluate $\hat{h}$ for eigenstates of (6,8) with $\epsilon \to \infty$ obtained analytically by Gunasekaraman and Venkataraman [47] to model cumulenes.

The product form of the helicality operator reads

$$\hat{h} = \frac{\mathrm{i}}{2}(\mathbb{T} - \mathbb{T}^\top) \otimes \hat{\sigma}_2, \tag{32}$$

where the matrix (5) has been used. Comparing with Eq. (26), we immediately see that the helicality operator commutes with the angular momentum operator,

$$[\hat{L}_z, \hat{h}] = 0.$$

The crucial difference between these two observables lies in the behavior under time reversal. While $\hat{L}_z$ changes sign, the real $\hat{h}$ is invariant under time reversal. Explicit form of the time-reversal operator is shown in Sec. III A.

The eigenstates of $\hat{h}$ are complex; they resemble "circularly-polarized" waves, as shown in Appendix A 5. In Appendix A 3, we show that the helicality operator commutes with chain Hamiltonian $\hat{H}_0$ up to the end group terms,

$$[\hat{H}_0, \hat{h}] = t(\mathbb{B}_1 - \mathbb{B}_N) \otimes \mathrm{i}\hat{\sigma}_2,$$

where $\mathbb{B}_N$ and $\mathbb{B}_1$ are defined in Eq. (11). It can be shown that when chains are closed into rings (periodic boundary condition), the commutator vanishes, and $\hat{H}_0$ has common eigenstates with $\hat{h}$ (Appendix A 4).

It is of interest to evaluate helicality for chains coupled to reservoirs. Using the notation of Eq. (14),

$$h(E_\mathrm{F}, V) = h(E_\mathrm{F}, 0) + \mathscr{O}(V),$$

and formula (19) yields

$$h(E_\mathrm{F}, 0) = \int_{-\infty}^{E_\mathrm{F}} \mathrm{Tr}[\hat{h}\hat{A}(E)]\mathrm{d}E, \tag{33}$$

and the quasiequilibrium response coefficient

$$\left.\frac{\partial h(E,0)}{\partial E}\right|_{E_\mathrm{F}} = \mathrm{Tr}[\hat{h}\hat{A}(E_\mathrm{F})]. \tag{34}$$

In stark contrast to the angular momentum, the equilibrium value of helicality can be finite. This should not come as a surprise, given that in our construction helicality of orbitals in isolated chains can be nonzero.

5. *Helicality operator in the continuum limit*

Before presenting extensive numerical analysis, we digress to perform a continuum limit of the helicality operator in order to lend extra plausibility to our definition of $\hat{h}$. The coordinate along the molecular backbone is chosen to be z and the carbons are located at na, a being the bond length. The Hückel wavefunction of the chain is here denoted by the column vector $\psi(z)$ with two entries $\psi_x(z)$ and $\psi_y(z)$, which are the projections on the $\mathrm{p}_{x,y}$ orbitals on the site z. The right-hand side of Eq. (29) in this fashion

reads

$$\frac{1}{2}[\psi_x^*(z)\psi_y(z+a) - \psi_y^*(z)\psi_x(z+a) + \text{c.c.}] = \frac{\mathrm{i}}{2}[\psi^\dagger(z)\,\hat{\sigma}_2\,\psi(z+a) \;+\; \text{c.c.}], \tag{35}$$

where matrix multiplication is implied in the second line. We can expand $\psi(z+a) = \psi(z) + a\partial_z\psi(z) + \mathcal{O}(a^2)$. If the wavefunction varies smoothly, second- and higher-order terms can be neglected; Eq. (35) becomes

$$\frac{\mathrm{i}a}{2}\{\psi^\dagger(z)\hat{\sigma}_2\partial_z\psi(z) - [\partial_z\psi^\dagger(z)]\hat{\sigma}_2\psi(z)\} = \frac{\mathrm{i}a}{2}\int[\psi^\dagger(z')\hat{\sigma}_2\delta(z-z')\partial_{z'}\psi(z') + \psi^\dagger(z')\hat{\sigma}_2\partial_{z'}\delta(z-z')\psi(z')]\mathrm{d}z'. \tag{36}$$

The second line follows from an integration of a Dirac's delta function; in the third line, we used integration by parts. The integral expression above offers the definition of the helicality density

$$\hat{h}(z) = \frac{\mathrm{i}}{2}\hat{\sigma}_2\{\partial_z, \delta(z-\hat{z})\} \tag{37}$$

$$= -\frac{m}{\hbar}\hat{\sigma}_2\hat{j}(z), \tag{38}$$

where we introduced the longitudinal particle current density operator $\hat{j}(z) := \frac{1}{2}\{\frac{\hat{p}_z}{m}, \delta(z-\hat{z})\}$, the anticommutator $\{,\}$, and the momentum operator $\hat{p}_z := -\mathrm{i}\hbar\partial_z$.

The integral of $\hat{h}(z)$ leads to a continuum representation of the helicality operator:

$$\hat{h} = \int \hat{h}(z)\mathrm{d}z = -\frac{1}{\hbar}\,\hat{p}_z\hat{\sigma}_2. \tag{39}$$

Identifying $\hat{L}_z = \hbar\hat{\sigma}_2$ [cf. Eq. (26)], we arrive at the important identity

$$\hat{h} = -\frac{1}{\hbar^2}\,\hat{p}_z\hat{L}_z. \tag{40}$$

This expression has the form (up to a factor) of the helicity operator $\hat{p}_z\hat{L}_z$ of a particle constrained to move along the z direction [51]. The prefactor contains $\hbar^{-2}$ because $\hat{h}$, with the continuum limit taken, has dimension 1 over length. The minus sign should not cause confusion: The left side of Eq. (40) quantifies the wavefunction shape and the right side an actual particle motion.

Notice that the $\hat{L}_z$ can be replaced by its real-space representation $-\mathrm{i}\hbar(\hat{x}\partial_y - \hat{y}\partial_x)$. This allows to employ the helicality operator beyond the Hückel theory, e.g., with a richer atom-centered basis. For instance, formula (40) can be utilized in *ab-initio* calculations, as an alternative to the nodal plane precession technique of Ref. [30].

Helicity encountered in Eq. (40) has a transparent geometrical meaning for planewaves: Such a state is helical when it has both angular and longitudinal momentum nonzero. A classical picture of a particle moving along a helix can be visualized. But helicity can be finite in standing waves, too. Standing waves are composed of pairs of planewaves, related by time reversal. Formally, $\psi \propto [|p,\uparrow\rangle + |-p,\downarrow\rangle]/\sqrt{2}$, where the arrows denote the angular momentum projection. Notice that $\langle\hat{L}_z\rangle$ and $\langle\hat{p}_z\rangle$ vanish for ψ. However, this is not true for $\langle\hat{L}_z\hat{p}_z\rangle$. A simple calculation shows that helicity is finite in ψ, although the linear and angular momenta vanish. Algebraically, this behavior is due to the product $\hat{p}_z\hat{L}_z$ commuting with the time-reversal operator, unlike the linear and angular momenta, which anticommute. Therefore, for isolated carbon chains, helical eigenstates (standing waves) have $\langle\hat{h}\rangle \neq 0$, although $\langle\hat{L}_z\rangle = 0$. Coupling to the reservoirs with steady-state current breaks time reversal; consequently, $\langle\hat{L}_z\rangle_{\text{res}} \neq 0$. In the continuum limit, the latter result must hold because of Eq. (40).

III. SYMMETRY ANALYSIS OF THE HAMILTONIAN AND THE OBSERVABLES

We show in Sec. III C that Models 1 and 2 enjoy an SL symmetry and explore its consequences for molecular orbitals of isolated chains. For chains coupled to leads, we derive antisymmetry relations of linear-response coefficients of helicality and angular momentum. These relations follow from SL symmetry in combination with time reversal. The presence of both symmetries—SL and time reversal—implies that both Models 1 and 2 belong to the symmetry class BDI of the tenfold classification [43,52].

Throughout this section, we set $t = t'$ for the sake of simplicity, although the main result—the effect of SL symmetry on angular momentum and helicality—remains valid when $t \neq t'$ or when hoppings are inhomogeneous.

A. Basic symmetries of the chains

We start with rather evident symmetries, the time-reversal invariance (TRI) and rotational symmetry. Implications of TRI are explored: vanishing equilibrium angular momentum and symmetrization of the angular momentum response coefficient.

1. Cylindrical symmetry

Carbon chains terminated by H– on both ends, such as the one shown in Fig. 2, enjoy full rotational invariance, C_∞, around the z axis. The commutator

$$[\hat{H}_0, \hat{L}_z] = 0$$

can be most easily derived from expressions (4,26). The loss of rotational symmetry that comes with end-group terms of Models 1 and 2 is a prerequisite for finite expectation value of angular momentum in chains with current flow.

2. Time reversal

An important role in the subsequent analysis of transport is played by the time-reversal operator $\hat{\Theta}$. We emphasize that the basis in which the Hückel model is written is real, i.e., the p orbitals are real harmonics. In the product form of operators, such as Eq. (26), the Pauli matrices do not represent spin, but a pseudospin, that does not invert sign upon time reversal. Consequently, the time-reversal operator reduces to complex conjugation $\mathcal{C}$,

$$\hat{\Theta} = \mathbb{I} \otimes \hat{\sigma}_0\,\mathcal{C} \;\equiv \mathcal{C}. \tag{41}$$

Hence, the following identities hold:

$$\{\hat{L}_z,\ \hat{\Theta}\} = 0, \quad [\hat{h}, \hat{\Theta}] = 0, \tag{42a}$$

showing a distinctively different behavior of helicality and angular momentum, already discussed in Secs. II B 4 and II B 5.

Since the Hamiltonian is real,

$$[\hat{H}, \hat{\Theta}] = 0, \tag{43}$$

with any end-group type.

To analyze the self-energies, we introduce the decomposition

$$\hat{\Sigma}(E) = \hat{\Delta}(E) - \frac{\mathrm{i}}{2}\hat{\Gamma}(E), \tag{44a}$$

$$\hat{\Delta}(E) := \frac{1}{2}[\Sigma(E) + \Sigma^\dagger(E)], \tag{44b}$$

$$\hat{\Gamma}(E) := \mathrm{i}[\hat{\Sigma}(E) - \hat{\Sigma}^\dagger(E)], \tag{44c}$$

where $\hat{\Gamma}(E)$ and $\hat{\Delta}(E)$ are hermitian by definition. From embedding theory [49], it can be shown that both quantities must be real if the leads are time-reversal invariant. Therefore,

$$[\hat{\Gamma}, \hat{\Theta}] = 0 \tag{45}$$

and $\hat{\Theta}\hat{\Sigma}(E) = \hat{\Sigma}^\dagger(E)\hat{\Theta}$. The above conditions for $\hat{\Sigma}(E)$ apply also to the left and right components, $\hat{\Sigma}_{\mathrm{L,R}}(E)$, separately. Finally, Eq. (17) brings us to the condition of time reversal of chains coupled to leads,

$$\hat{\Theta}\hat{G}^{(\mathrm{R})}(E) = \hat{G}^{(\mathrm{A})}(E)\hat{\Theta}. \tag{46}$$

3. *Consequences of time-reversal invariance (TRI) for observables*

It is known that some observables change sign upon time reversal, others don't [Eq. (42) exemplifies this]. This is reflected, quantum-mechanically, by the (anti-) commutation with $\hat{\Theta}$,

$$\hat{\Theta}\hat{O} = \pm\hat{O}\hat{\Theta}, \tag{47}$$

where the sign is sometimes called a "signature" [45]. Let us inspect the equilibrium expectation value [Eq. (19)] of an observable $\hat{O}$. $\hat{A}(E)$ is hermitian by definition [see Eq. (20)], but TRI [Eq. (46)] restricts it to be real and symmetric:

$$\hat{\Theta}\hat{A}(E) = \hat{A}(A)\hat{\Theta}.$$

We insert the identity $\hat{\Theta}^2 = \hat{1}$ into the trace [Eq. (19)] and apply commutation rules,

$$\mathrm{Tr}[\hat{\Theta}\hat{\Theta}\hat{O}\hat{A}(E)] = \pm\mathrm{Tr}[\hat{\Theta}\hat{O}\hat{A}(E)\hat{\Theta}].$$

The signs correspond to the ones in Eq. (47). The right $\hat{\Theta}$ can be dropped as it operates on real wavefunctions and the left one can be replaced by the conjugation of the resulting trace. But the latter is real, which makes us conclude that

$$\mathrm{Tr}[\hat{O}\hat{A}(E)] = \pm\mathrm{Tr}[\hat{O}\hat{A}(E)] \tag{48}$$

and $O(E_\mathrm{F}, 0) = \pm O(E_\mathrm{F}, 0)$. Consequently, observables that change sign upon time reversal have a vanishing expectation value in equilibrium in a TRI system. This is the case for the angular momentum

$$L_z(E_\mathrm{F}, 0) = 0.$$

Helicality, on the other hand, does not vanish when $V = 0$.

B. Sublattice symmetry in cumulenes

Both Models 1 and 2 are endowed with the SL symmetry, which has important implications not only for helicality, but also for angular momentum. The SL symmetry has different form in the two cases and we start with the simpler case, Model 1. Here, the SLs are constructed according to the parity of each carbon along the chain. Hence, the bipartite lattice in cumulenes is analogous to the notion of bipartite lattices in planar sp^2 hybridized carbons ("graphenoids"). Both p orbitals on the same atom belong to the same SL. On the ends, only the p orbital, pertaining to the π system, counts. To demonstrate that algebraically, we introduce the operator that flips signs on odd-numbered carbons,

$$\hat{P} := \sum_{n=1}^{N}(-1)^n[|y_n\rangle\langle y_n| + |x_n\rangle\langle x_n|] = \mathbb{P}\otimes\hat{\sigma}_0, \tag{49}$$

where the diagonal matrix

$$\mathbb{P} := \begin{pmatrix} -1 & 0 & 0 & \cdots \\ 0 & +1 & 0 & \cdots \\ 0 & 0 & -1 & \cdots \\ \vdots & \vdots & \vdots & \ddots \end{pmatrix} = \mathrm{diag}(-1, +1, -1, +1, \ldots) \tag{50}$$

is defined. The SL symmetry is a statement that with $\hat{H} = \hat{H}_0 + \hat{H}_1 + \hat{H}_N$ and Eqs. (4), (12), and (8) it holds that

$$\{\hat{H},\ \hat{P}\} = 0 \quad \text{(Model 1)} \tag{51}$$

when $\epsilon \to \infty$.

To prove that, we first show that the "bulk" part of the Hamiltonian anticommutes with $\hat{P}$, namely,

$$\{\hat{H}_0,\ \hat{P}\} = 0, \tag{52}$$

with Eq. (4). This follows from

$$\{\mathbb{T}, \mathbb{P}\} = \{\mathbb{T}^\top,\ \mathbb{P}\} = 0 \tag{53}$$

[see also Eq. (5)]. Next, the left boundary term, site 1 with Eq. (8), delivers the result

$$\{\hat{H}_1,\ \hat{P}\} = -2\epsilon|x_1\rangle\langle x_1|. \tag{54}$$

In the limit $\epsilon \to \infty$, wavefunctions of the π orbital system have a vanishing weight on the $|x_1\rangle$ site [53]. Therefore, the relevant matrix elements of Eq. (54) vanish. Analogously,

$$\{\hat{H}_N,\ \hat{P}\} = 2\epsilon(-1)^N\,\mathbb{B}_N \otimes \left[\hat{R}(\theta_\mathrm{T}) \cdot \begin{pmatrix} 1 & 0 \\ 0 & 0 \end{pmatrix} \cdot \hat{R}^\top(\theta_\mathrm{T})\right], \tag{55}$$

where Eqs. (7), (8), and (12) have been used. The square braces enclose a 2×2 matrix. It is a projector on a linear combination of $|x_N\rangle$, $|y_N\rangle$ states that is truncated from the π system. Again, Eq. (55) has vanishing matrix elements within the π system, and Eq. (51) is proven.

It is not hard to show that

$$\{\hat{h},\ \hat{P}\} = 0 \tag{56a}$$

using Eq. (53). Figure 4 offers a geometric view of the anticommutator: The $\hat{P}$ inverts the phase of the p orbitals of one member of the bond. If one of the components of vector $\boldsymbol{P}$ flips sign, so does the cross product and ϕ. Further

identities

$$\hat{P}^\dagger = \hat{P}, \tag{56b}$$

$$\hat{P}^2 = 1, \tag{56c}$$

$$[\hat{L}_z, \hat{P}] = 0, \tag{56d}$$

will be instrumental for deriving consequences of the SL symmetry. Equation (56d) says that a simultaneous inversion of x and y axes does not change the sense of rotation around z.

It can be expected that in more complete models of cumulenes, the SL symmetry holds approximately, only. One example of the symmetry-breaking term is the on-site potential of the p_y orbital on the first carbon, which can be slightly different from the carbons in the middle of the chain. The effect of this term is small because of the small energy and because of locality. We look at this in more depth in the case of oligoynes.

C. A $\hat{Q}$ symmetry in oligoynes

We show that Model 2 also enjoys an anticommutator relation of form (51), with $\hat{P}$ replaced by an operator $\hat{Q}$. The meaning of the anticommutator is less straightforward than in cumulenes. In Sec. III D, we show that a suitable basis change transforms the Hamiltonian into a form where the SL is revealed.

We define an operator

$$\hat{Q} \coloneqq \sum_{n=1}^{N} (-1)^n [|y_n\rangle\langle x_n| - |x_n\rangle\langle y_n|], \tag{57}$$

which, up to signs, exchanges locally the p_x and p_y orbitals. In the tensor product form, $\hat{Q} = -\mathrm{i}\mathbb{P} \otimes \hat{\sigma}_2$, with Eq. (50).

The central result of this work is that for the Hamiltonian $\hat{H}$ with the parametrization (10), we have

$$\{\hat{H},\ \hat{Q}\} = 2\mathrm{i}(a^{(1)}\mathbb{B}_1 - (-1)^N a^{(N)}\mathbb{B}_N) \otimes \hat{\sigma}_2, \tag{58}$$

where $\mathbb{B}_{1,N}$ are defined in Eq. (11). Moreover, it holds that

$$[\hat{L}_z, \hat{Q}] = 0, \tag{59}$$

$$\{\hat{h},\ \hat{Q}\} = 0. \tag{60}$$

Let us start with the "bulk" term,

$$\{\hat{H}_0,\ \hat{Q}\} = -\mathrm{i}t\{\mathbb{T} + \mathbb{T}^\top,\ \mathbb{P}\} \otimes \hat{\sigma}_2 = 0,$$

using Eqs. (4) and (53). Anticommutation rules $\{\hat{\sigma}_i,\ \hat{\sigma}_j\} = 2\hat{\sigma}_0\delta_{ij}$ $(i > 0,\ j > 0)$ imply for the end-group terms

$$\begin{aligned}\{\hat{H}_1,\ \hat{Q}\} &= (-1)^1 a^{(1)}\mathbb{B}_1 \otimes \{\hat{\sigma}_0,\ -\mathrm{i}\hat{\sigma}_2\} \\ &= 2\mathrm{i}a^{(1)}\mathbb{B}_1 \otimes \hat{\sigma}_2 \\ \{\hat{H}_N,\ \hat{Q}\} &= (-1)^N a^{(N)}\mathbb{B}_N \otimes \{\hat{\sigma}_0,\ -\mathrm{i}\hat{\sigma}_2\} \\ &= (-1)^{N+1} 2\mathrm{i}a^{(N)}\mathbb{B}_N \otimes \hat{\sigma}_2.\end{aligned}$$

Grouping the three Hamiltonian terms together, we prove Eq. (58). Using Eq. (53), the relation

$$\{(\mathbb{T} - \mathbb{T}^\top) \otimes \hat{\sigma}_2,\ \mathbb{P} \otimes \hat{\sigma}_2\} = 0$$

follows. Therefore, Eq. (60) holds in view of definition (32). On the other hand, commutator (59) holds because both $\hat{L}_z$ and $\hat{Q}$ are proportional to $\hat{\sigma}_2$ and $[\mathbb{I}, \mathbb{P}] = 0$ [see Eq. (26)]. The unitarity relations will prove useful

$$\hat{Q}^{-1} = -\hat{Q} = \hat{Q}^\dagger, \tag{61}$$

which follow from idempotency $\hat{\sigma}_2^2 = \hat{\sigma}_0$.

Concluding, the Hamiltonian of Model 2 anticommutes with $\hat{Q}$ up to boundary terms on the right-hand side of Eq. (58). We refer to the vanishing of these terms as SL symmetry of Model 2. Namely,

$$a^{(1)} = a^{(N)} = 0 \quad \text{(SL symmetry)}. \tag{62}$$

The Hamiltonian terms proportional to $a^{(1,N)}$ have the $\hat{\sigma}_0$ form; these terms offset the on-site potential on the end sites equally for each p orbital. Therefore, they do not induce helicality and may be seen as irrelevant for current-induced angular momentum. For the discussion of the generation of helical orbitals, the $\hat{\sigma}_0$ terms can be taken to be zero. In Appendix B, we show that these terms lead to weak violation of the SL symmetry, only.

D. A sublattice representation of Model 2

We show that a suitable change of basis transforms the the Hamiltonian to a matrix form which reveals a bipartite lattice structure. To achieve this, we bring the operator $\hat{Q}$ to a diagonal form. It follows that the transformation diagonalizes $\hat{\sigma}_2$. Incidentally, because of Eq. (26), this is the transformation to angular momentum eigenstates. Let

$$\hat{U} \coloneqq \mathbb{I} \otimes \exp -\mathrm{i}\frac{\pi}{4}\hat{\sigma}_1 = \mathbb{I} \otimes \frac{1}{\sqrt{2}}(\hat{\sigma}_0 - \mathrm{i}\hat{\sigma}_1)$$

map to a (complex) basis, which can be labeled

$$(|\uparrow_1\rangle, |\downarrow_1\rangle, |\uparrow_2\rangle, |\downarrow_2\rangle, \ldots) \tag{63}$$

[cf. Eq. (1)] where the arrow is a shorthand for the orbital angular momentum projection, $\pm\hbar$, and the subscript labels the atom. Then, $\hat{U}\hat{Q}\hat{U}^\dagger = -\mathrm{i}\mathbb{P} \otimes \hat{\sigma}_3$ is a diagonal matrix. Apart from the factor $+\mathrm{i}$, the diagonal elements multiply wavefunction values on every other point of the "lattice" by -1. Specifically, SL B, receiving the minus signs, is seen to be

$$\text{SL B} = (|\downarrow_1\rangle, |\uparrow_2\rangle, |\downarrow_3\rangle, |\uparrow_4\rangle, \ldots),$$

and SL A is the remainder (see Fig. 5).

Next, with Eq. (10), the end-term transforms

$$\hat{U}\hat{H}_1\hat{U}^\dagger = \mathbb{B}_1 \otimes [a^{(1)}\hat{\sigma}_0 + b^{(1)}\hat{\sigma}_1 - c^{(1)}\hat{\sigma}_2]$$

and similarly for $\hat{H}_N$. Notice that there are no $\hat{\sigma}_3$ terms after the transformation. Moreover, $\hat{H}_0$ does not change its matrix form, because it commutes with angular momentum. Summarizing, the Hamiltonian, including end terms, transforms to

$$\begin{aligned}\tilde{\hat{H}} \coloneqq \hat{U}\hat{H}\hat{U}^\dagger &= -t(\mathbb{T} + \mathbb{T}^\top) \otimes \hat{\sigma}_0 \\ &+ \mathbb{B}_1 \otimes [a^{(1)}\hat{\sigma}_0 + b^{(1)}\hat{\sigma}_1 - c^{(1)}\hat{\sigma}_2] \\ &+ \mathbb{B}_N \otimes [a^{(N)}\hat{\sigma}_0 + b^{(N)}\hat{\sigma}_1 - c^{(N)}\hat{\sigma}_2].\end{aligned}$$

When the condition (62) holds, $\tilde{\hat{H}}$ is free from matrix elements that operate on basis functions of the same SL (see Fig. 5 for a graphical representation). If the basis set [Eq. (63)]

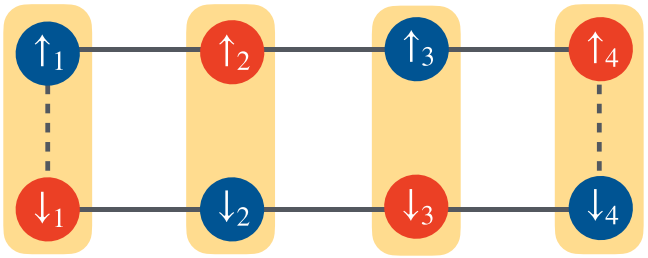

FIG. 5. Scheme of the SL symmetric model of a carbon chain with 4 atoms in the representation of angular momentum eigenstates. On each atom (yellow box), there are two $\hat{L}_z$ eigenstates with $L_z = \pm\hbar$, labeled by the arrow. Blue (red) color denotes the emergent sublattice A (B) of the model. Solid lines represent the nearest-neighbor "hopping" terms in the Hamiltonian, equal to $-t$. Dashed lines represent the couplings within the end groups. Atoms of the same SL do not couple. The couplings effectively arrange into a ring.

is reordered so that all A-lattice elements come before all B-lattice ones, the matrix of $\widehat{\hat{H}}$ has the block structure

$$\begin{pmatrix} 0 & \mathbf{w} \\ \mathbf{w}^\dagger & 0 \end{pmatrix}, \tag{64}$$

with only the nondiagonal blocks $\mathbf{w}$, $\mathbf{w}^\dagger$ nonzero. Concluding, in the representation of $\hat{L}_z$ eigenstates, the hidden SL symmetry uncovers itself.

Hamiltonians of form (64) are also called *chiral*, or, possessing chiral symmetry, in relativistic physics, in mesoscopic physics of bipartite lattice systems and other areas of quantum physics [52,54]. To avoid confusion, we stress that it is not related to structural chirality of the molecule.

The helicity operator transforms to

$$\hat{U}\hat{h}\hat{U}^\dagger = \frac{\mathrm{i}}{2}(\mathbb{T} - \mathbb{T}^\top) \otimes \hat{\sigma}_3,$$

which allows for a transparent view of its eigenstates, namely, as direct products of angular momentum and "linear" momentum eigenstates.

E. Sublattice symmetric self-energy

To study the consequences of SL symmetry for nonequilibrium situations with current, SL symmetry must be assumed for the self-energy. We begin by exploring the structure of the Green's function of isolated chains, denoted by $\hat{g}^{(\mathrm{R})}(E)$. This is Eq. (16) with $\hat{\Sigma}$ replaced by a negative imaginary infinitesimal, $-\mathrm{i}\hat{1}0^+$. We can convince ourselves that

$$\begin{aligned} \hat{Q}\,\hat{g}^{(\mathrm{R})}(E)^{-1} &= \hat{Q}[(E+\mathrm{i}0^+)\hat{1} - \hat{H}] = \\ &= \quad [(E+\mathrm{i}0^+)\hat{1} + \hat{H}]\hat{Q} = \\ &= -[(-E-\mathrm{i}0^+)\hat{1} - \hat{H}]\hat{Q} = \\ &= -\hat{g}^{(\mathrm{A})}(-E)^{-1}\hat{Q}, \end{aligned}$$

where, as before, we assumed SL symmetry in Model 2 and used Eq. (17). Multiplication of the above equation from the right by $\hat{g}^{(\mathrm{R})}(E)$ and from the left by $\hat{g}^{(\mathrm{A})}(-E)$ and flipping signs yields $\hat{g}^{(\mathrm{A})}(E)\hat{Q} = -\hat{Q}\hat{g}^{(\mathrm{R})}(-E)$. This is a reformulation of SL symmetry [Eqs. (58) and (62)] for isolated chains. We now define the SL symmetry of chains coupled to reservoirs by the condition

$$\hat{Q}\hat{G}^{(\mathrm{R})}(E) = -\hat{G}^{(\mathrm{A})}(-E)\hat{Q}. \tag{65}$$

By repeating the calculation in the paragraph above with the full Green's function, the condition (65) implies

$$\hat{Q}\hat{\Sigma}(E) = -\hat{\Sigma}^\dagger(-E)\hat{Q}. \tag{66}$$

Using Eq. (44),

$$\hat{Q}\hat{\Delta}(E) = -\hat{\Delta}(-E)\hat{Q}, \tag{67a}$$

$$\hat{Q}\hat{\Gamma}(E) = +\hat{\Gamma}(-E)\hat{Q}. \tag{67b}$$

Self-energy, representing the coupling to the leads, should fulfill these conditions in order to preserve SL symmetry. The components $\hat{\Gamma}_{\mathrm{L}}(E)$, $\hat{\Gamma}_{\mathrm{R}}(E)$ inherit these conditions as well. We remark that local coupling has not been assumed here [unlike, e.g., in Eq. (13)]. Evidently, the simplified cylindrical wide-band Ansatz [Eq. (13)], used in numerical calculations, satisfies these conditions. Moreover, any constant contribution to $\hat{\Delta}(E)$, which has the same structure as the SL-symmetric end-group terms [Eq. (10) with Eq. (62)], also fulfills Eq. (67). Ultimately, every realistic lead is going to break the SL symmetry. When the self-energy is obtained from a microscopic description of the contacts (e.g., *ab initio*), the expressions put forth here can be used to identify the SL-perturbing terms.

F. Implications of sublattice symmetry for observables

For both Models 1 and 2, the SL symmetry has the algebraic form of the anticommutator [cf. Eq. (58) with Eq. (51)]. The $\hat{Q}$ operator takes on the role of $\hat{P}$ when we go from Models 1 to 2 [compare Eq. (56) with Eqs. (59) and (60)]. There is only one algebraic difference, the presence of the minus sign in Eq. (61) (unlike: $\hat{P}^{-1} = \hat{P}$). The minus in Eq. (61) disappears if one drops the factor i in the definition of $\hat{Q}$, but we shall not do it. We conclude that the consequences of SL symmetry are going to be identical for Model 1 and 2, specifically, for the energy spectrum, helicity and angular momentum. These consequences are shown in the following. We focus on Model 2 (oligoynes) for concreteness.

1. Isolated chains—spectrum and helicality

Let us have a Hamiltonian $\hat{H}$ of Model 2 with the eigenvalues and eigenstates from

$$\hat{H}|\psi\rangle = E|\psi\rangle.$$

Then, $\hat{H}\hat{Q}|\psi\rangle = -\hat{Q}\hat{H}|\psi\rangle = -E\hat{Q}|\psi\rangle$ if condition (62) holds. Hence, $\hat{Q}|\psi\rangle$ is a "partner" eigenstate of $\hat{H}$ corresponding to eigenenergy $-E$. These are the Coulson-Rushbrooke pairs, mentioned in the Introduction. For instance, $\hat{Q}$ maps highest occupied molecular orbital (HOMO) to lowest unoccupied molecular orbital (LUMO) when the chain is half-filled with electrons. When the Fermi level coincides with $E = 0$, single-particle excitations (of this effectively noninteracting system) are *particle-hole symmetric*.

Moreover, for the expectation value of helicity in an arbitrary state $|\varphi\rangle$ it holds that

$$\langle\hat{Q}\varphi|\hat{h}|\hat{Q}\varphi\rangle = -\langle\varphi|\hat{Q}^\dagger\hat{Q}\hat{h}|\varphi\rangle = -\langle\varphi|\hat{h}|\varphi\rangle, \tag{68}$$

where Eqs. (60) and (61) have been invoked. We conclude that the Hamiltonian eigenstates are mirror symmetric with respect to energy and antisymmetric with respect to their expectation value of helicity when SL symmetry is present. For example, HOMO and LUMO have opposite winding sense, and so do HOMO−1 and LUMO+1 (half filling). These identities of the eigenstates and eigenvalues of Model 2 apply equally to Model 1 (cumulenes). One only needs to replace $\hat{Q}$ for $\hat{P}$ in the derivations.

Discussion of previous works on cumulenes. In Refs. [26,27], molecular orbitals of various cumulenes were calculated *ab initio*. The helical HOMOs and LUMOs, portrayed therein, have always opposite winding senses. The same was observed by Gunasekaran and Venkataraman, who employed a Hückel model [47], equivalent to our Model 1. This phenomenon can now be rationalized by the SL symmetry.

2. Transport: reciprocity of linear response coefficients

The SL symmetry (62), combined with time-reversal invariance, implies certain identities of response functions, introduced in Sec. II B. These relations can be classified as Onsager reciprocity relations [55–57]. We prove them within the Landauer formalism below. A discussion of the impact of molecular vibrations is offered in Appendix E.

Transmission. To prove the consequences of the (anti)commutators on the transmission probability $\mathfrak{T}(E)$, we insert into the trace formula (24) the identity $\hat{1} = -\hat{Q}\hat{Q}$ [see Eq. (61)] and commute one $\hat{Q}$ to the right, using Eqs. (65) and (67) and cyclic invariance of the trace. Hence,

$$\begin{aligned}\mathfrak{T}(E) &= -\mathrm{Tr}[\hat{Q}\hat{Q}\hat{G}^{(\mathrm{R})}(E)\hat{\Gamma}_{\mathrm{L}}(E)\hat{G}^{(\mathrm{A})}(E)\hat{\Gamma}_{\mathrm{R}}(E)]\\ &= \mathrm{Tr}[\hat{Q}\hat{G}^{(\mathrm{A})}(-E)\hat{\Gamma}_{\mathrm{L}}(-E)\hat{Q}\hat{G}^{(\mathrm{A})}(E)\hat{\Gamma}_{\mathrm{R}}(E)]\\ &= -\mathrm{Tr}[\hat{Q}\hat{G}^{(\mathrm{A})}(-E)\hat{\Gamma}_{\mathrm{L}}(-E)\hat{G}^{(\mathrm{R})}(-E)\hat{\Gamma}_{\mathrm{R}}(-E)\hat{Q}]\\ &= \mathrm{Tr}[\hat{G}^{(\mathrm{A})}(-E)\hat{\Gamma}_{\mathrm{L}}(-E)\hat{G}^{(\mathrm{R})}(-E)\hat{\Gamma}_{\mathrm{R}}(-E)].\end{aligned}$$

Since the above formula looks like a transmission of some time-reversed system, we insert there $\hat{\Theta}^2 = \hat{1}$ under the trace and proceed commuting as before,

$$\begin{aligned}\mathfrak{T}(E) &= \mathrm{Tr}[\hat{\Theta}\hat{\Theta}\hat{G}^{(\mathrm{A})}(-E)\hat{\Gamma}_{\mathrm{L}}(-E)\hat{G}^{(\mathrm{R})}(-E)\hat{\Gamma}_{\mathrm{R}}(-E)]\\ &= \mathrm{Tr}[\hat{\Theta}\hat{G}^{(\mathrm{R})}(-E)\hat{\Gamma}_{\mathrm{L}}(-E)\hat{\Theta}\hat{G}^{(\mathrm{R})}(-E)\hat{\Gamma}_{\mathrm{R}}(-E)]\\ &= \mathrm{Tr}[\hat{\Theta}\hat{G}^{(\mathrm{R})}(-E)\hat{\Gamma}_{\mathrm{L}}(-E)\hat{G}^{(\mathrm{A})}(-E)\hat{\Gamma}_{\mathrm{R}}(-E)\hat{\Theta}].\end{aligned}$$

Equations (45) and (46) have been used. Above, the right $\hat{\Theta}$ operates on real wavefunctions and the left one can be factored before the trace (as a conjugation), which is real. We have achieved a standard result:

$$\mathfrak{T}(E) = \mathfrak{T}(-E). \tag{69}$$

Indeed, it is known that transmission of a time-reversal and SL—symmetric system is even; see, e.g., Ref. [57], where the statement is derived within a family of *Onsager* reciprocity theorems.

Helicality and angular momentum. Now we are in a place to prove the identities for the linear response coefficients of helicality and angular momentum [Eqs. (27) and (34)]. These response coefficients are odd functions of the Fermi energy $E = E_{\mathrm{F}}$, namely,

$$\frac{\partial h(E,0)}{\partial E} = -\frac{\partial h(-E,0)}{\partial E}, \tag{70a}$$

$$\left.\frac{\partial L_z(E,V)}{\partial V}\right|_{V=0} = -\left.\frac{\partial L_z(-E,V)}{\partial V}\right|_{V=0}. \tag{70b}$$

To prove the latter relation, we start with the respective trace expression

$$\mathrm{Tr}\{\hat{L}_z\,\hat{G}^{(\mathrm{R})}(E)[\hat{\Gamma}_{\mathrm{L}}(E) - \hat{\Gamma}_{\mathrm{R}}(E)]\hat{G}^{(\mathrm{A})}(E)\},$$

and insert $\hat{1} = -\hat{\Theta}^2\hat{Q}^2$, in full analogy to the treatment of the transmission. Additional minus sign appears: $\hat{L}_z$ commutes with $\hat{Q}$ but anticommutes with $\hat{\Theta}$.

Finally, from

$$\hat{Q}[\hat{G}^{(\mathrm{R})}(E) - \hat{G}^{(\mathrm{A})}(E)] = [\hat{G}^{(\mathrm{R})}(-E) - \hat{G}^{(\mathrm{A})}(-E)]\hat{Q},$$

we infer that

$$\hat{Q}\hat{A}(E) = \hat{A}(-E)\hat{Q}$$

[see the definition of $\hat{A}(E)$ in Eq. (20)]. Combining with Eq. (60), we have $\mathrm{Tr}[\hat{Q}\hat{Q}\hat{h}\hat{A}(E)] = -\mathrm{Tr}[\hat{Q}\hat{h}\hat{A}(-E)\hat{Q}]$; henceforth, Eq. (70a) is proven. This identity does not refer to a nonequilibrium and the derivation does not involve time reversal; it is therefore not an Onsager reciprocity.

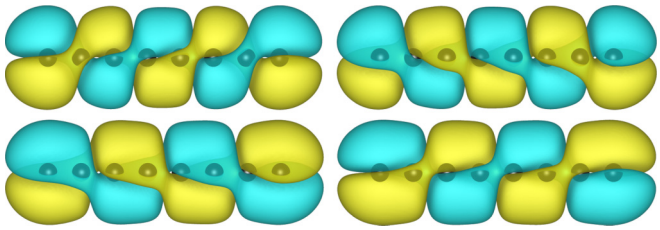

FIG. 6. The frontier orbitals of carbon chains ($N = 8$) with the end groups parametrized with $\epsilon = 0.5t$, $\theta_{\mathrm{T}} = 45°$: LUMO + 1, LUMO (upper row), and HOMO − 1, HOMO (lower row). The winding sense of the orbitals is alternating with increasing orbital energy. Images generated with VESTA [58].

IV. HELICALITY IN PERTURBATION THEORY

To motivate the subsequent perturbative analysis, we plot in Fig. 6 few orbitals with energies around the center of the band for $\theta_{\mathrm{T}} = 45°$, $N = 8$, $\epsilon = 0.5t$ (Model 2). The SL symmetry is only broken weakly (see Appendix B) and the band center is located between HOMO and LUMO . The portrayed molecular orbitals display winding directions consistent with Eq. (68). Furthermore, the sign of helicality alternates with increasing orbital energy, which we inspect here analytically. For $|\epsilon| \ll t$, we can employ perturbation theory in $\hat{H}_{\mathrm{pert}} = \hat{H}_1 + \hat{H}_N$. The $\hat{H}_0$ is a reference Hamiltonian, representing unsubstituted oligoynes. Because $\hat{H}_0$ has the p_x, p_y subsystems decoupled, the eigenstates are doubly degenerate. We list the unperturbed eigenstates and eigenenergies in Appendix C 2.

The first-order energy corrections are

$$E^{(1)}_{\mu\pm} = \frac{2\epsilon}{N+1}\sin^2\left(\frac{\mu\pi}{N+1}\right)(1 \pm \cos(\theta_{\mathrm{T}})), \tag{71}$$

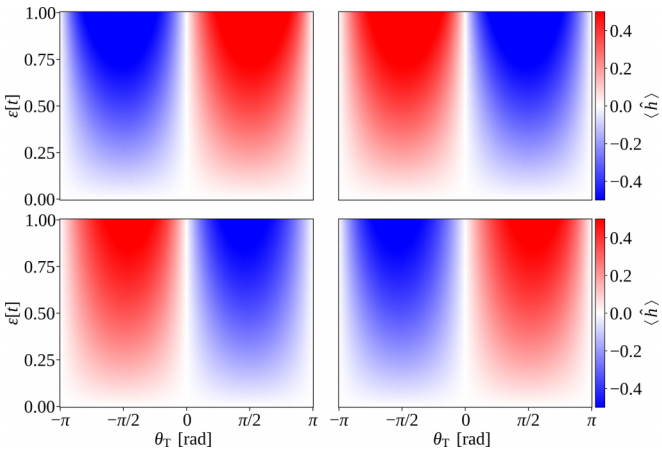

FIG. 7. The helicity $\langle\hat{h}\rangle$ as a function of θ_T and ϵ: HOMO–1, HOMO (bottom row), and LUMO +1, LUMO (top row) for $N = 8$.

where $\mu \in \{1, 2, 3, \ldots, N\}$ is the quantum number of the unperturbed eigenstates and $\pm$ label transverse chain modes (see Appendix C or Ref. [59] for details).

The expectation value of helicity, to first order, results in

$$h^{(1)}_{\mu,\pm} = \pm\frac{4\epsilon}{t(N+1)^2}\sin(\theta_T) \times \sum_{\substack{\nu \\ \mu+\nu=\text{odd}}} \frac{\sin^2\left(\frac{\mu\pi}{N+1}\right)\sin^2\left(\frac{\nu\pi}{N+1}\right)}{\left(\cos\left(\frac{\mu\pi}{N+1}\right)-\cos\left(\frac{\nu\pi}{N+1}\right)\right)^2} \quad (72)$$

(see Appendix C or Ref. [59] for derivation). The last formula shows that helicity can be broken down into several factors: The term $\sin(\theta_T)$ shows that the π orbital is twisted due to the boundary terms. Helicity vanishes for angles $\theta_T = 0, \pm\pi$. In our model, these special angles imply a planar (D_{2h}) symmetry, which excludes helical eigenstates, as discussed by Hendon *et al.* [26]. The terms included after the summation in (72) account for the influence of the variation of the longitudinal wavefunction phase onto the precession of $\boldsymbol{P}_n$. Importantly, comparing Eqs. (71) and (72), the originally degenerate p_x, p_y doublets always split into pairs of states with opposite helicalities. The only exceptions are $\theta_T = 0, \pm\pi$ (no helical orbitals). Additionally, for $\theta_T = \pm\frac{1}{2}\pi$ the pair of orbitals is degenerate; helicity can be removed by an orthogonal transformation. The alternating helicity was observed already by Gunasekaran and Venkataraman [47] for $\epsilon = \infty$; here, we show that it reproduces in the perturbative regime as well and point out its physical consequence (for angular momentum) in the next section. Figure 13 shows that the perturbation theory works qualitatively well for both energy and helicality even when $\epsilon \approx t$.

To inspect the alternation further, we show the helicity beyond perturbative regime from numerical diagonalization in Fig. 7, showing a monotonous dependence of $\langle\hat{h}\rangle$ on ϵ which is free from sign changes. Naturally, a large ϵ can lead to level crossings, which break the alternation pattern. Such crossings occur first near the bottom and top of the band. The states near the center of the band will still preserve alternation for ϵ up to $\approx t$. In view of the Ref. [47], the alternation re-establishes in the entire spectrum for large $\epsilon \to \infty$, representing cumulenes (Model 2 goes to Model 1). Finally, we remark that the chain characteristics discussed here analytically and numerically are robust against moderately strong substitutional disorder, we refer to Appendix D for details.

V. CHAINS COUPLED TO RESERVOIRS: NUMERICAL RESULTS

Coupling the carbon chains to reservoirs under bias results in circular currents that wind around the axis. It is natural to expect that the associated circular currents produce an orbital angular momentum. Here, we explore in detail the relation between the latter and helicality.

A. Angular dependence

To relate the emergence of angular momentum to orbital helicality, we show various spectral densities of embedded chains in Fig. 8. The program and generated data are available in Ref. [60].

The first row shows the transmission function [Eq. (24)]. For $\eta = 0.01t$ (left column), the quasidegenerate doublets are clearly visible. Their angular dependence is consistent with the behavior of eigenenergies of isolated chains [Fig. 13 and Eq. (71)]. In the strong coupling regime, $\eta = 0.5t$ (right column), the resonances are much wider, as expected. For the subsequent analysis, the following distinction becomes useful: In the weak coupling, only the states within the doublet can spectrally overlap, while in the strong coupling, states from the nearby doublets may admix.

The second row presents the equilibrium coefficient, $\partial h(E_F, V = 0)/\partial E_F$. The plots can be understood by recalling the analytic result (71), or Fig. 13, for the splitting of $p_{x,y}$ doublets into pairs of opposite helicity. For both strong and weak couplings, helicality vanishes trivially at $\theta_T = 0, \pi$ and at $\theta_T = \frac{\pi}{2}$, because this is the degeneracy point—the transmission resonances overlap completely and no net helicality is generated. The sectors $\theta_T \in \langle 0, \frac{\pi}{2}\rangle$ and $\langle\frac{\pi}{2}, \pi\rangle$ differ only by the sign, because at the degeneracy point the two quasidenegenerate states interchange. Helicality also vanishes for $E_F \approx 0$, when the Fermi level is in the middle of the HOMO-LUMO gap ("half filling"). At weak coupling, when only the quasidegenerate pairs have spectral overlap, $\partial h(E_F, 0)/\partial E_F$ is vanishingly small for most E_F, except near transmission resonances. This is because the pairs have opposite helicality and their integrated effect on the equilibrium helicality cancels. Also in the strong coupling regime do we find sign alternation across the energies: for fixed θ_T, there is a sign change (node) at the original doublet energies and another node in the larger gaps between doublets (off-resonant energies). We notice that for $0 < \theta_T < \frac{\pi}{2}$ and $E_F < 0$ the latter node is pushed down in energy from the midpoint energy of the larger gap. In other words, in the quadrant $0 < \theta_T < \frac{\pi}{2}$ and $E_F < 0$, the negative $h(E_F, 0)$ occupies more area.

The bottom row of Fig. 8 presents the angular momentum. Crucially, for $\theta_T = 0, \pi/2, \pi$ helicality vanishes ("linear polarization"); consequently, angular momentum vanishes as well. The most important observation is that $\partial L_z(E_F, V = 0)/\partial V$ is an odd function with respect to the middle of the HOMO-LUMO gap ($E_F = 0$). The details of the angular

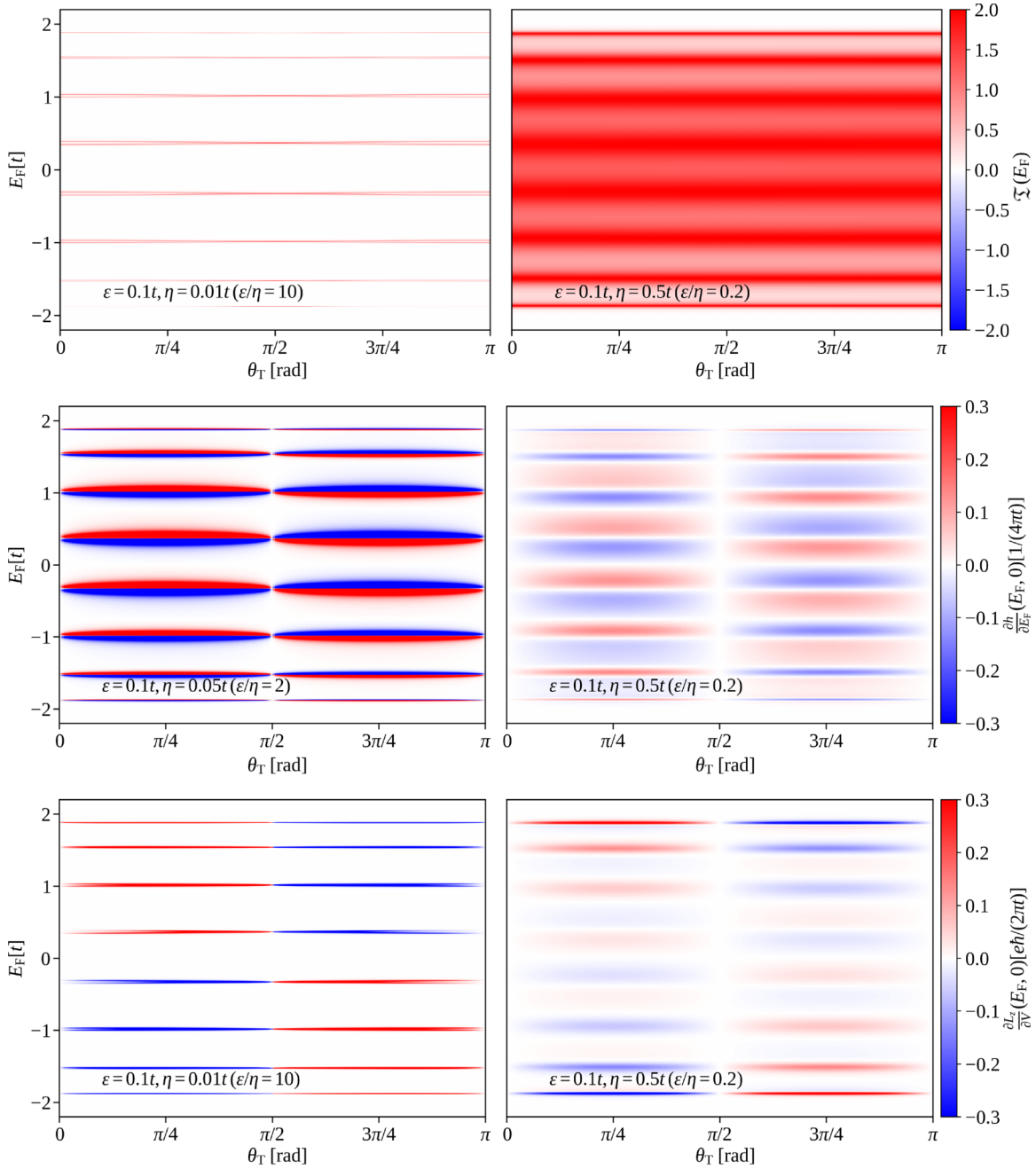

FIG. 8. Color maps of various observables for the chain with $N = 8$ sites coupled to reservoirs with $\eta = 0.01t$ (left column) and $\eta = 0.5t$ (right column) for twist angles $\theta_T > 0$, with $\epsilon = 0.1t$. Top row: transmission function $\Upsilon(E)$, second row: equilibrium helicity ($\partial h/\partial E_F$), and third row: angular momentum response ($\partial L_z/\partial V$).

momentum response differ at strong and weak couplings, respectively. For $\eta = 0.5t$, the angular momentum response follows closely the helicity response; in particular, its signs and nodes. Loosely speaking, the angular momentum inherits the alternating behavior (as a function of E_F) from helicity. In weak coupling, for a fixed θ_T, the behavior of $\partial L_z(E_F, V = 0)/\partial V$ is markedly different from $\partial h(E_F, V = 0)/\partial E_F$. For $\eta = 0.01t$, the pairs of perturbatively split resonances (doublets) manifest as doublets in $\partial L_z(E_F, V = 0)/\partial V$, however, with equal sign. For a fixed θ_T, the sign change occurs markedly at E_F. The change of the $\partial L_z(E_F, V = 0)/\partial V$ peak structure between the two regimes (strong and weak coupling) is explored in the next section.

These numerical results exemplify the preceding analytical analysis: (1) Helicity alternates with energy, resulting in Eq. (72). We add to this observation the following remark: When time reversal is broken by the electric current, the alternating helicity translates into the alternation of angular momentum, with E_F. (2) The symmetry relations (70) and (69) manifest in Fig. 8. The SL symmetry, although approximate, is a powerful concept to rationalize the energy dependence of the observables. We inspect the departure of SL symmetry in more detail in the subsequent sections.

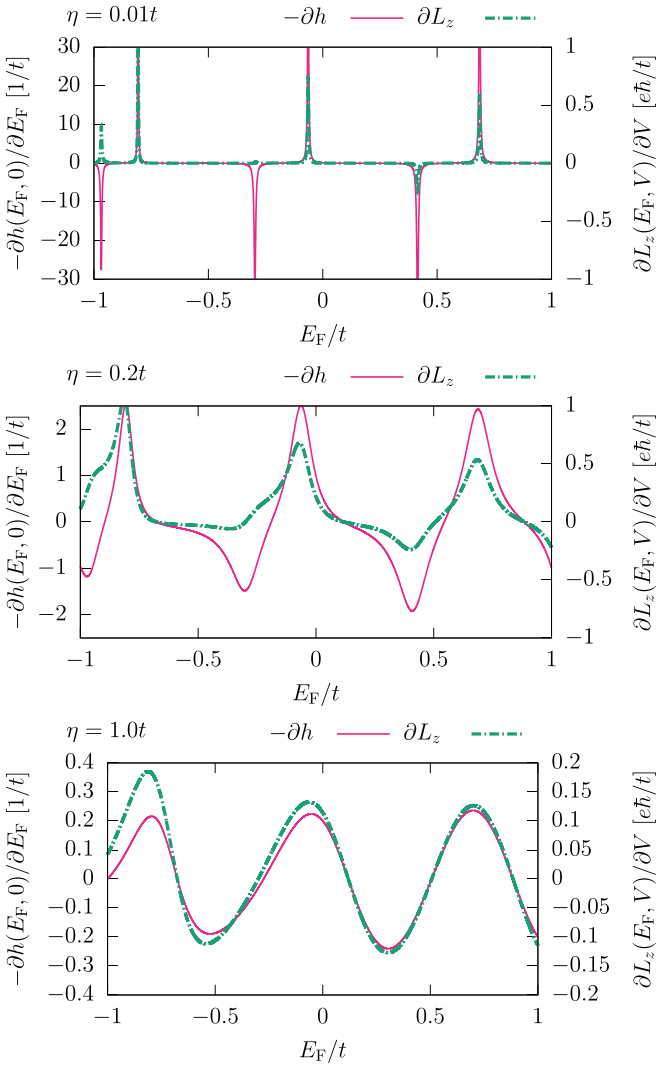

FIG. 9. Comparison of helicality, $(\partial h/\partial E_F)$, (solid magenta lines) with angular momentum, $(\partial L_z/\partial V)$, (dot-dashed green) responses for couplings $\eta = 0.01t$ (top), $0.2t$ (middle), and $\eta = 1t$ (bottom). Notice that helicality is multiplied by a minus sign. The parameters are $N = 8, \epsilon = 0.1t, \theta_T = \frac{\pi}{4}$.

B. From weak to strong coupling

To reveal the interdependence of helicality and angular momentum, we fix here the twist angle to $\theta_T = \frac{\pi}{4}$ and plot the linear responses in Fig. 9 for various coupling strengths.

We first notice that $\partial L_z(E_F, V = 0)/\partial V$ and $\partial h(E_F, V = 0)/\partial E_F$ are mostly of opposite signs. This can be rationalized using the continuum form [Eq. (40)]. Since the z coordinate increases from the left end group toward the right one, and particles flow from left to right when V is positive, the linear momentum, on average, must be positive. The minus sign in Fig. 9 thus reflects the minus sign in Eq. (40). Weak SL symmetry breaking manifests here by the E_F dependencies being "almost odd" with respect to energy $E \approx 0.1t$.

The noteworthy observation is that the "negative" helicality and angular momentum follow closely each other, when the coupling is strong. Since $\partial h(E_F, V = 0)/\partial E_F$ can be understood from the helicality of chains in isolation (helicality of molecular orbitals), helicality becomes a proxy

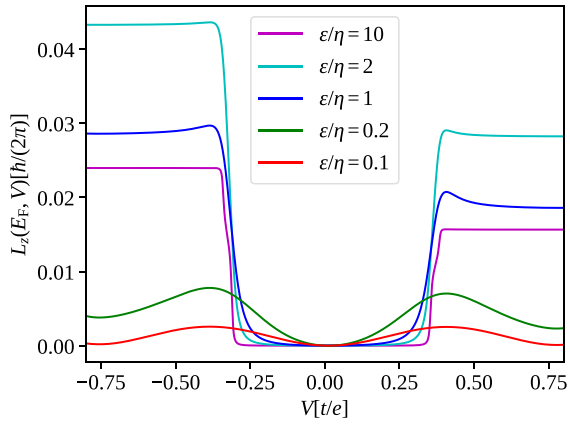

FIG. 10. The expectation value of the angular momentum as a function of V for $E_F = 0$. Parameters: $\theta_T \approx -44.66°, N = 8, \epsilon = 0.1t$.

for the resulting angular momentum upon the current flow, in nonequilibrium. This correspondence seems to weaken for weak coupling, but still seems to hold near $E = 0$.

C. Angular momentum beyond linear response

Equation (70b) states that when particle-hole symmetry is present, i.e., there is SL symmetry and the Fermi level is in the band center, $E_F = 0$, angular momentum is zero in linear response in the voltage bias. Remarkably, the sign change of $\partial L_z(E_F, V = 0)/\partial V$ at $E_F = 0$ has a peculiar physical manifestation beyond linear response. For definiteness, we assume that the bias drops entirely on the left lead, $\mu_L = E_F + eV$ while $\mu_R = E_F$. This description is used to model scanning-probes with molecules on surfaces; the molecule equilibrates with the surface (here the right lead). To express the nonlinear response of $L_z(E_F, V)$, we invoke Eqs. (21) and (22) and recognize the relation

$$L_z(E_F, V) = \frac{1}{e}\int_{E_F}^{E_F+eV} \frac{\partial L_z(E, V = 0)}{\partial V} \mathrm{d}E. \qquad (73)$$

The latter is even in V. Angular momentum does not reverse sign when the current flow reverses.

The connection to helicality offers an intuitive understanding of this result. When the bias is positive, the tunneling current "probes" molecular orbitals that are different when the bias is reversed; e.g., these can be the HOMO and the LUMO. Due to SL symmetry, these orbitals have opposite helicality. If current runs in the same direction, intuitively, these orbitals carry opposite angular momentum as well. A classical picture of a particle traveling along screws is invoked. However, the sign of the current is reversed with V and this implies that $L_z(E_F = 0, V)$ does not change sign. This phenomenology holds true not only for Model 2 (oligoynes), but also Model 1 (cumulenes), as established in Sec. III B. Fig. 10 showcases these ideas numerically for different coupling strengths.

The figure reveals another remarkable feature of the voltage dependence of the induced angular momentum. When $|eV|$ exceeds the transmission resonance energy $\sim 0.35t$ of the frontier orbital, $L_z(E_F, V)$ decreases. This decrease is stronger at strong coupling. The observation can be rationalized in virtue of the discussion in the preceding section and Fig. 9.

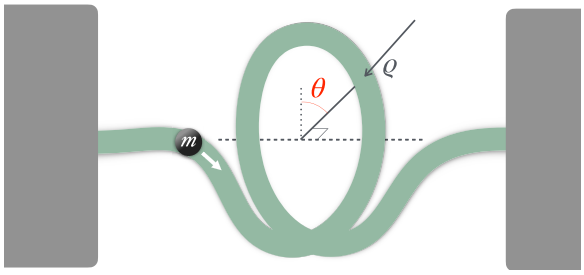

FIG. 11. A minimal model of current-induced rotation with a molecular junction represented by a helical tube. Here, the helix emerges from one lead, it revolves approximately $N = 1$ times and connects to the other lead. With respect to the central axis (dashed line), the initial and final radius of the trajectory is zero, and the radius attains its maximum ϱ. A particle of mass m can move freely through the tube. The particle does not carry angular momentum, except when it is in the central helical segment. The tube can rotate freely around the axis—its orientation $\theta(t)$ is a dynamic variable.

Since orbital helicality alternates, raising the voltage beyond the resonance energy admixes the subsequent orbital and the latter contributes to the integral (73) with angular momentum of an opposite sign. An experimental-based study [18,19] also reported a decrease of rotation for large bias, despite an increase of the current.

We end by noting that the action of SL symmetry-breaking terms [$\propto \hat{\sigma}_0$ in Eq. (10)] is evident in Fig. 10. The difference in the large $|V|$ values of $L_z(E_F, \pm V)$ is $\approx$20% of average value $(L_z(E_F, V) + L_z(E_F, -V))/2$. Notice that the SL-breaking terms have the same energy ϵ as the helicality and angular-momentum—inducing terms, in the chosen parametrization. Yet, the SL breaking does not change the qualitative picture.

VI. DISCUSSION AND OUTLOOK

Previous sections predict that there is a finite electronic orbital angular momentum (EOAM) in a situation with a steady-state current through the carbon chain (axle). The EOAM is here linked to helical orbitals, but this is not a necessary condition—it is natural to expect the EOAM in molecular junctions with axial chirality. Here, we discuss the implications of the steady-state EOAM on the dynamics of the molecular rotor.

Review of a minimal model. We invoke here a minimal model of the current-induced molecular rotation introduced by Korytár and Evers in Ref. [25]. This minimal model relies on angular momentum conservation, which is respected by quantum effects as well. Let us recall the essence of this model for the convenience of the reader. Consider source and drain connected by a narrow helical tube (representing the molecular junction) of the form shown in Fig. 11. Next, a particle (electron) can move freely along the tube, being constrained by the walls of the tube, only. A single scattering event, with the electron being transported from the source to the drain inertially, without acceleration from an external field, is envisioned. The rotor is still before this process. The electron acquires an EOAM in the tube, and this is compensated by the angular momentum of the tube, $\mathfrak{M}\dot{\theta}$, where $\mathfrak{M}$ is the rotor's moment of inertia. Because the particle's angular momentum is zero in the source and drain, there is no angular momentum of the rotor before and after the scattering. Yet, the rotor is left turned by an angle after the incident. The angle is

$$\Delta\theta = \pm\frac{2m\pi\langle\varrho^2\rangle N}{\mathfrak{M}}, \tag{74}$$

where m is the particle (electron) mass, N is approximately the number of turns of the helix, and $\langle\varrho^2\rangle$ is the average squared radius of the helix. The right-hand side does not depend on dynamical variables, such as scattering time and the EOAM. It only depends on the geometry and the mass ratio. We emphasize that the sign is determined by the chirality—it is opposite to the sign of EOAM during the transport. There is a torque when the electron enters the helix—for without it there would be no turn—and an opposite torque that stops the rotation when the electron leaves the helix. The mechanism induces rotation even if there is a potential barrier.

Application to chains with helical orbitals. We propose here that several outcomes of the minimal model apply to the carbon axles, connecting rotor and stator moieties (as shown in Fig. 1), and steady-state EOAM. If the rotation is free (the potential barrier is low), a constant angular velocity $\dot{\theta}$ is expected with steady-state current. This is because of a current flow: particles entering and leaving the carbon axle boost the θ.

An order-of-magnitude estimate of the boost $\Delta\theta$ per electron can be estimated by setting $\mathfrak{M} \approx M\langle R^2\rangle$, with the averaged radius of the rotor R:

$$\Delta\theta \approx 10\frac{m}{M}\frac{\langle\varrho^2\rangle}{\langle R^2\rangle}. \tag{75}$$

If $m/M \approx 10^{-5}$ (for a few atoms) and the ratio of variances is 10^{-2}, $\Delta\theta \approx 10^{-6}$ rad. We have assumed $2\pi N \approx 10$ here. A steady-state current scenario involves many electrons passing from source to drain. If the electrons are assumed independent, the current of 1 nA would induce full rotation in $\approx 10^{-4}$ s. The value of this estimate is that it provides an upper bound, because, e.g., other tunneling pathways and inelastic effects have been ignored.

To study the functionality of helical orbitals for molecular motors for specific applications, a more detailed description, including, e.g., dissipation and current-induced noise, is needed. More realistic models involve potential barriers [25] and semi-classical dynamics [22,61–63] that can involve *ab initio* details [64] for specific molecular designs.

Structural versus orbital chirality. The direction of rotation is determined by the sign of the EOAM, which in turn is determined by orbital helicality. The direction of rotation can be independent on the sign of the current, in view of Sec. V C. Such a molecular motor would operate as a galvano-mechanical rectifier. This behavior can be contrasted with helix-shaped molecular wires, e.g., DNA, or chiral carbon nanotubes: There the OAM with respect to the molecular axis must change sign with the current reversal. This is dictated by the *structural chirality*. Carbynes and cumulenes own helical orbitals whose helicality changes

as a function of energy, allowing the galvano-mechanical rectification.

Effects of spin-orbit coupling (SOC). While the SOC is weak in linear carbon chains, we would like to point out that interesting behavior can happen when one end group contains a heavier element with sizable SOC (Si, Pt; see Ref. [65] for more examples). When bias voltage is applied, this element can translate the OAM of the carbon chain into a spin current. This opens a possibility of chirality-induced spin-selective phenomena [34,66] with unusual behavior under current reversal.

VII. CONCLUSIONS

We have shown that carbon chains with helical orbitals lead to finite expectation values of electronic angular momentum, when these chains are coupled to reservoirs as molecular junctions. To make this relation more precise, we have quantified helicality of molecular orbitals by introducing a hermitian operator. For small twists and long chains, the expectation value of the operator equals an average orbital twist angle per bond.

We have elaborated several implications of SL symmetry for helicality and angular momentum. For the specific case of oligoynes, the SL symmetry is hidden in the sense that it is not straight-forwardly identified from the Hamiltonian of the Hückel theory. We have shown that molecular orbitals, whose energies are located symmetrically around band center, have opposite helicality.

For chains coupled to leads with bias voltage V, the angular momentum response coefficient has a node at the band center, as a consequence of Onsager reciprocity. In the nonlinear regime, we show that this behavior can lead to the angular momentum not changing sign with the current reversal. We propose an application as a molecular motor with a rectifying electromechanical response. In this context, we remark that circulating currents also generate a magnetic field and its detection was suggested earlier in Ref. [67].

Finally, we have clarified the connection between helical orbital shape, brought about and discussed in chemistry, and the helicity observable from the relativistic Dirac theory. In the continuum limit, helicity, and helicality (defined here) are identical, up to a natural constant.

ACKNOWLEDGMENTS

We thank Jan Wilhelm for helpful discussions in the early stage of the project. We are indebted to Lukas Gerhard for help with writing of the manuscript. We acknowledge the support of Czech Science Foundation (GAČR) through Grant No. 22-22419S, the support of Charles University through GAUK (ID: 366222) fellowship and funding by the German Research Foundation (DFG) as part of the German Excellence Strategy—EXC3112/1—533767171 (Center for Chiral Electronics) and CRC 1277 (Project No. 314695032, subproject A03P), and RTG 2905 (Project No. 502572516).

DATA AVAILABILITY

The data that support the findings of this article are openly available [60].

APPENDIX A: SOME PROPERTIES OF THE HELICALITY OPERATOR

We elaborate on certain aspects of helicality defined in this work. We give an alternative geometric picture in Appendix A 1. Then, in Appendix A 2 we evaluate helicality for cumulene eigenstates given elsewhere. We derive the commutator with the Hamiltonian in Appendix A 3 and finally diagonalize the helicality operator in Appendix A 5.

1. Geometric view of helicality with a classical particle on a helix

Suppose that we have a helix, such that if we travel distance $2\pi P$ along, we complete one turn exactly. Therefore, the change of a polar angle of a point on the helix is $\phi = \frac{z}{P}$ where z is the length of the arc described by the point. The rate of change of the polar angle per distance is therefore

$$\frac{\partial \phi}{\partial z} = \frac{1}{P}. \tag{A1}$$

We can apply this idea to the precessing $\boldsymbol{P}_n$ vectors from Sec. II B 4. There, the nodal plane of the p orbitals may not be turning uniformly and therefore we choose to focus on the average rate of rotation instead. Furthermore, we investigate the sine of the polar angle, as defined in Fig. 4. We associate the rate of change $\frac{1}{\tilde{P}}$ (per bond) with the following expression:

$$\frac{1}{\tilde{P}} := \frac{1}{N-1} \sum_{n=1}^{N-1} \frac{\boldsymbol{P}_n \times \boldsymbol{P}_{n+1}}{|\boldsymbol{P}_n||\boldsymbol{P}_{n+1}|} \tag{A2}$$

(since $\boldsymbol{P}_n \times \boldsymbol{P}_{n+1} = \mathbf{e}_z |\boldsymbol{P}_n||\boldsymbol{P}_{n+1}| \sin\phi$).

Assuming that the wavefunction's weight on each site is approximately the same, we put

$$|\boldsymbol{P}_n|^2 \approx \frac{1}{N}, \tag{A3}$$

and hence

$$\frac{1}{\tilde{P}} \approx \frac{N}{N-1} \sum_{n=1}^{N-1} \boldsymbol{P}_n \times \boldsymbol{P}_{n+1} \approx \sum_{n=1}^{N-1} \boldsymbol{P}_n \times \boldsymbol{P}_{n+1} \tag{A4}$$

for large N. The right-hand side, by definition, is the expectation value of the helicality operator. The left-hand side is the average sine of the angle of precession per bond.

2. Helicality of cumulene's eigenstates

Analytic expression for π orbitals of cumulenes is given in Ref. [47]. In our notation, they are eigenstates of Eq. (6) with end-group terms [Eq. (8)] and $\epsilon \to \infty$. These eigenstates can be written in the form

$$\psi_m = \boldsymbol{R}\left(\frac{\theta_T}{2}\right) \cdot \begin{pmatrix} \cos\phi \cos(km+\delta) \\ \sin\phi \sin(km+\delta) \end{pmatrix} r, \tag{A5}$$

for the sites $1 \leqslant m \leqslant N-1$ (i.e., excluding end groups). In the above equation, the two components denote the p_x and p_y projections; in our notation, $\psi_m \equiv \boldsymbol{P}_m$. The r is a normalization factor, the ϕ is the so-called ellipticity angle, δ is the initial phase of the molecular orbital, and k is its wave number. It can be seen that the wavefunction represents an ellipsis in a two-dimensional space. Helicality is then associated there with nontrivial values of $\phi \neq \pm\frac{\pi}{2}, 0$.

In the spirit of Sec. II B 4, we evaluate the axial component of $\boldsymbol{P}_m \times \boldsymbol{P}_{m+1}$ [Eq. (28)]. The global rotation $\boldsymbol{R}(\frac{\theta_T}{2})$ does not affect the result, which simplifies to

$$\begin{aligned}\tilde{h}_m = r^2 \sin\phi\cos\phi\{&\cos(km+\delta)[\sin(km+\delta)\cos(k)\\ &+\cos(km+\delta)\sin(k)]\\ &-\sin(km+\delta)[\cos(km+\delta)\cos(k)\\ &-\sin(km+\delta)\sin(k)]\} = \tfrac{1}{2}r^2\sin(k)\sin(2\phi). \end{aligned} \quad \text{(A6)}$$

Since $0 \leqslant k \leqslant \frac{\pi}{2}$, the sign of $\tilde{h}_m$ equals the sign of $\sin(2\phi)$. The sign of ϕ described the sense of winding in Gunasekaran *et al.* Concluding, our operator yields the winding sense consistently with the latter reference. Importantly, helicality adopts nonzero expectation values except for $\phi = \pm\frac{\pi}{2}, 0$.

Simplification occurs for $\phi = \mp\frac{\pi}{4}$, when vectors $\boldsymbol{P}_m$ draw a circle clockwise or anticlockwise. Using Eq. (A5) directly and estimating $r^2 \approx 2/N$ [from normalization of eigenstates of $\hat{H}_0$ (C11)], we have

$$\tilde{h}_m \approx \mp\frac{1}{N}\sin(k).$$

The expectation value of $\hat{h}$ is obtained by summing over bonds, which yields

$$\langle\hat{h}\rangle \approx \mp\frac{N-1}{N}\sin(k).$$

For large N, we get an average bond twisting angle $\mp k$.

3. Commutator of helicality with $\hat{H}_0$

The commutator of the helicality operator $\hat{h} = \frac{1}{2}(\mathbb{T} - \mathbb{T}^\top)\otimes \mathrm{i}\hat{\sigma}_2$ with $\hat{H}_0$ can be expanded as follows:

$$\begin{aligned}[\hat{H}_0, \hat{h}] &= -t((\mathbb{T}+\mathbb{T}^\top)\cdot(\mathbb{T}-\mathbb{T}^\top))\otimes \mathrm{i}\hat{\sigma}_0\hat{\sigma}_2\\ &\quad - t((\mathbb{T}-\mathbb{T}^\top)\cdot(\mathbb{T}+\mathbb{T}^\top))\otimes \mathrm{i}\hat{\sigma}_2\hat{\sigma}_0\\ &= -t[\mathbb{T}+\mathbb{T}^\top, \mathbb{T}-\mathbb{T}^\top]\otimes \mathrm{i}\hat{\sigma}_2. \end{aligned} \quad \text{(A7)}$$

With the matrix elements

$$\begin{aligned}(\mathbb{T})_{jk} &= \delta_{j,k-1},\\ (\mathbb{T}^\top)_{jk} &= \delta_{j-1,k}, \end{aligned} \quad \text{(A8)}$$

we obtain

$$\begin{aligned}[\mathbb{T}+\mathbb{T}^\top, \mathbb{T}-\mathbb{T}^\top]_{jk} &= \sum_{l=1}^{N}(\delta_{j,l-1}+\delta_{j-1,l})(\delta_{l,k-1}-\delta_{l-1,k})\\ &\quad -(\delta_{j,l-1}-\delta_{j-1,l})(\delta_{l,k-1}+\delta_{l-1,k})\\ &= \sum_{l=1}^{N} 2\delta_{j-1,l}\delta_{l,k-1} - 2\delta_{j,l-1}\delta_{l-1,k}\\ &= 2\sum_{l=1}^{N}\delta_{j,l+1}\delta_{l+1,k} - 2\sum_{l=0}^{N-1}\delta_{j,l}\delta_{l,k}\\ &= 2\sum_{l=2}^{N+1}\delta_{j,l}\delta_{l,k} - 2\sum_{l=1}^{N-1}\delta_{j,l}\delta_{l,k}\\ &= 2(\delta_{j,N+1}\delta_{N+1,k} + \delta_{j,N}\delta_{N,k} - \delta_{j,1}\delta_{1,k}) \end{aligned}$$

and since j and k are never larger than N, we have the expression

$$[\hat{H}_0, \hat{h}] = (-t)(\mathbb{B}_N - \mathbb{B}_1)\otimes \mathrm{i}\hat{\sigma}_2, \quad \text{(A9)}$$

where $(\mathbb{B}_l)_{jk} = \delta_{jl}\delta_{lk}$.

4. Extension to carbon rings

Expression (A9) suggests the idea that helicality is an integral of motion when chains (hard-wall boundaries) are closed into rings with periodic boundary conditions (PBC) (for example, Garner *et al.* investigate helical orbitals in cyclic systems [29]). To validate this idea mathematically, we introduce the ring Hamiltonian

$$\hat{H}_0^{\mathrm{PBC}} = -t(\mathbb{S}+\mathbb{S}^\top)\otimes\hat{\sigma}_0, \quad \text{(A10)}$$

where

$$(\mathbb{S})_{jk} = \delta_{j,k \bmod N+1}.$$

Here, $k \bmod N$ is the remainder of k after integer division by N (k modulo N). $\hat{H}_0^{\mathrm{PBC}}$ is essentially $\hat{H}_0$ plus additional matrix elements that allow for hybridization ("hopping") of carbon 1 with carbon N. The helicality operator needs to be amended as well in order to account for the twist of the 1–N bond,

$$\hat{h}^{\mathrm{PBC}} = \frac{\mathrm{i}}{2}(\mathbb{S}-\mathbb{S}^\top)\otimes\hat{\sigma}_2.$$

The commutator in PBCs becomes

$$\begin{aligned}\left[\hat{H}_0^{\mathrm{PBC}}, \hat{h}^{\mathrm{PBC}}\right] &= \frac{-\mathrm{i}t}{2}[\mathbb{S}+\mathbb{S}^\top, \mathbb{S}-\mathbb{S}^\top]\otimes\hat{\sigma}_2\\ &= \frac{-\mathrm{i}t}{2}([\mathbb{S}^\top,\mathbb{S}]-[\mathbb{S},\mathbb{S}^\top])\otimes\hat{\sigma}_2\\ &= \frac{-\mathrm{i}t}{2}([\mathbb{S}^\top,\mathbb{S}]+[\mathbb{S}^\top,\mathbb{S}]^\top)\otimes\hat{\sigma}_2. \end{aligned}$$

So, we only need to evaluate the elements of $[\mathbb{S}^\top, \mathbb{S}]$

$$\begin{aligned}([\mathbb{S}^\top,\mathbb{S}])_{jk} = \sum_{m=1}^{N}&(\delta_{j\bmod N+1,m}\delta_{m,k\bmod N+1}\\ &-\delta_{j,m\bmod N+1}\delta_{m\bmod N+1,k}). \end{aligned}$$

Since both m and $m\bmod N+1$ produce integers from 1 to N for all m from 1 to N, the summation evaluates to

$$([\mathbb{S}^\top,\mathbb{S}])_{jk} = \delta_{j\bmod N+1,k\bmod N+1} - \delta_{j,k}.$$

Again, since j and k are both within 1 and N, the first Kronecker delta reduces to δ_{jk}, which leads to

$$([\mathbb{S}^\top,\mathbb{S}])_{jk} = 0 \quad \text{(A11)}$$

and hence

$$\left[\hat{H}_0^{\mathrm{PBC}}, \hat{h}^{\mathrm{PBC}}\right] = 0. \quad \text{(A12)}$$

5. Helicality eigenstates

The eigenvectors of $\hat{h}$, determined analytically, read

$$\langle n|n_{hl}, n_{hsl}, m\rangle = Z_{n_{hsl}} \begin{pmatrix} \mathrm{i}^{n_{hsl}} & \sin\left(\frac{n_{hl}\pi}{N+1}\right) \\ \mathrm{i}^{2n_{hsl}} & \sin\left(\frac{2n_{hl}\pi}{N+1}\right) \\ \vdots & \\ \mathrm{i}^{Nn_{hsl}} & \sin\left(\frac{Nn_{hl}\pi}{N+1}\right) \end{pmatrix} \otimes \begin{pmatrix} \frac{1}{\sqrt{2}} \\ \frac{\mathrm{i}m}{\sqrt{2}} \end{pmatrix}, \tag{A13}$$

where the quantum numbers take on integer values $n_{hl} \in \{1, 2, ..., N/2\}$, $m, n_{hsl} \in \{-1, 1\}$. Notice that the commutator $[\hat{L}_z, \hat{h}] = 0$ is reflected here: Both operators are diagonalized simultaneously; $\hbar m$ is actually the angular momentum projection; the $\hat{L}_z$ eigenstate is the rightmost factor in the above expression.

The corresponding eigenvalues of $\hat{h}$ are

$$h = -n_{hsl} m \cos\left(\frac{n_{hl}\pi}{N+1}\right). \tag{A14}$$

We observe that both real and imaginary parts of $\langle n|n_{hl}, n_{hsl}, m\rangle$ have form of circularly polarized states. Namely, the associated $\boldsymbol{P}_n$ moves on a circle (notice the power of the imaginary i), making a $\pm 90°$ turn over each bond. The circle's radius is scaled by the sine factor on each site.

APPENDIX B: IMPACT OF SUBLATTICE SYMMETRY BREAKING ON THE WAVEFUNCTIONS

We employ a test Hamiltonian of an $N = 4$ chain,

$$\hat{H}_{\text{test}} = \hat{H}_0 + \mathbb{B}_1 \otimes \left(\frac{\epsilon}{2}\hat{\sigma}_3 + \delta\hat{\sigma}_0\right) + \mathbb{B}_4 \otimes \left(\frac{\epsilon}{2}\hat{\sigma}_1 + \delta\hat{\sigma}_0\right), \tag{B1}$$

where $\hat{H}_0$ is given in Eq. (4) and the end-group terms are expressed as in Eq. (12). Equation (58) implies that the terms proportional to δ break SL symmetry. It can be shown that the end-group terms are rotated with respect to each other by $\theta_{\text{T}} = \frac{\pi}{4}$, in the spirit of Eq. (7).

Let us have the normalized eigenvectors $|i\rangle (i = 1, \ldots, 8)$ of $\hat{H}_{\text{test}}$ ordered with increasing energy. When $\delta = 0$, $|i\rangle$ and $|8 - i\rangle$ are related by $|i\rangle = \hat{Q}|8 - i\rangle$, up to a phase factor—possibly a minus sign. This motivates the definition of the measure of SL symmetry breaking

$$\Delta_i \coloneqq \min \| \, |i\rangle \pm \hat{Q}|8 - i\rangle \, \| \tag{B2}$$

for a given orbital pair. The min and $\pm$ are due to the phase ambiguity and the delimiters indicate that vector norm is to be taken.

We show Δ_i for HOMO and HOMO-1 in Fig. 12. It grows approximately linearly for small δ and the curve is concave, because Δ_i is bounded from above. Since the SL breaking terms are local, Δ_i remains small unless δ grows beyond $\sim 0.5t$. In particular, for the model of chains with H_3C- end groups, with $\epsilon = 0.2$ and $\delta = \epsilon/2 = 0.1$, both Δ's are smaller than 0.1.

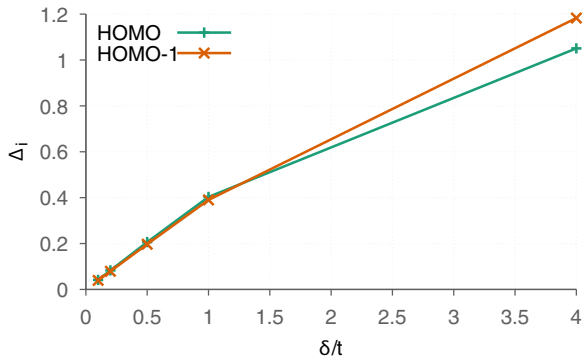

FIG. 12. Norm of the difference of a Hamiltonian eigenvector, $|i\rangle$, and its SL mirror partner—see the definition in Appendix B. δ/t controls the strength of SL breaking terms in the Hamiltonian of a four-carbon chain [Eq. (B1) with $\epsilon = 0.2$].

APPENDIX C: PERTURBATION THEORY FOR END-GROUP TERMS

The perturbative treatment of end groups [Eqs. (6), (7), and (9)] requires paying special attention to the degeneracies; we review the most important formulæ in these two subsections. The reader can find more details in the thesis [59].

1. First-order corrections to observables

Suppose that we have an unperturbed Hamiltonian $\hat{H}^0$ with eigenstates $|\psi^0_{\mu l}\rangle$ of $\hat{H}^0$ coming in degenerate $M-$tuples

$$\hat{H}^0|\psi_{\mu l}\rangle = E^0_\mu |\psi^0_{\mu l}\rangle, \quad l \in \{1, 2, ..., M\}, \tag{C1}$$

where μ is the nondegenerate index and l enumerates eigenstates within a degenerate subspace. We assume that a perturbation $\hat{V}$ fully lifts the degeneracy of the system. To the first order, an established procedure [68,69] is to choose a different basis

$$|\phi^0_{\mu j}\rangle = \sum_{l=1}^{M} |\psi^0_{\mu l}\rangle \alpha_{\mu, l j}, \tag{C2}$$

which diagonalizes the matrix elements of $\hat{V}$ for each μ, i.e.,

$$\forall \mu : \langle \phi^0_{\mu l}|\hat{V}|\phi^0_{\mu l'}\rangle = \tilde{V}_{\mu l, \mu l}\delta_{l l'}, \tag{C3}$$

where $\tilde{V}_{\mu l, \mu l} = \langle \phi^0_{\mu l}|\hat{V}|\phi^0_{\mu l}\rangle$ and $\delta_{l l'}$ is the Kronecker delta. In such basis, the perturbation series goes as

$$\begin{aligned} &(\hat{H}^0 + \hat{V})\left(|\phi^0_{\mu l}\rangle + |\phi^1_{\mu l}\rangle + \cdots\right) \\ &\quad = \left(E^0_\mu + E^1_{\mu l} + \cdots\right)\left(|\phi^0_{\mu l}\rangle + |\phi^1_{\mu l}\rangle + \cdots\right). \end{aligned} \tag{C4}$$

Subtracting the zeroth order and leaving only terms to first order leads to

$$\left(\hat{H}^0 - E^0_\mu\right)|\phi^1_{\mu l}\rangle = \left(E^1_{\mu l} - \hat{V}\right)|\phi^0_{\mu l}\rangle. \tag{C5}$$

Scalar product shows that $E^1_{\mu l} = \tilde{V}_{\mu l, \mu l}$, which is also the eigenvalue of eigenvectors used for diagonalization of the matrix elements of $\hat{V}$.

By a general scalar product with $\langle \phi^0_{\mu l'}|$ of the right-hand side of Eq. (C5), we find that the resulting vector has no

contribution in the degenerate space

$$\langle\phi^0_{\mu l'}|(E^1_{\mu l}-\hat{V})|\phi^0_{\mu l}\rangle = E^1_{\mu l}\delta_{ll'} - \tilde{V}_{\mu l',\mu l} = 0 \tag{C6}$$

and therefore we can retrieve the first-order corrections to the state as

$$|\phi^1_{\mu l}\rangle = \sum_{\nu\neq\mu}\sum_{l'=1}^{M}\frac{(-\tilde{V}_{\nu l',\mu l})}{E^0_\nu - E^0_\mu}|\phi^0_{\nu l'}\rangle. \tag{C7}$$

This is a standard result of the perturbation theory, but we explicitly separated the sum over the (originally) degenerate subspaces.

The corrections to observables (such as helicity $\hat{h}$) are given as

$$h^0_{\mu l} + h^1_{\mu l} + \cdots = \big(\langle\phi^0_{\mu l}| + \langle\phi^1_{\mu l}| + \cdots\big)\hat{h}\big(|\phi^0_{\mu l}\rangle + |\phi^1_{\mu l}\rangle + \cdots\big), \tag{C8}$$

where the zeroth order $h^0_{\mu l} = \langle\phi^0_{\mu l}|\hat{h}|\phi^0_{\mu l}\rangle$.

To the first order, we then have (similar as in the nondegenerate case in Ref. [69])

$$h^1_{\mu l} = \langle\phi^1_{\mu l}|\hat{h}|\phi^0_{\mu l}\rangle + \langle\phi^0_{\mu l}|\hat{h}|\phi^1_{\mu l}\rangle \tag{C9}$$

$$= \sum_{\nu\neq\mu}\sum_{l'=1}^{M}\frac{(-\tilde{V}_{\nu l',\mu l})^* h_{\nu l',\mu l} + (-\tilde{V}_{\nu l',\mu l})h_{\mu l,\nu l'}}{E^0_\nu - E^0_\mu}. \tag{C10}$$

2. Application to oligoynes with methyl end groups

The Hamiltonian $\hat{H}_0$ has eigenstates of the form (for even N) [47]

$$|\psi^0_{\mu l}\rangle = Z\begin{pmatrix}\sin\left(\frac{\mu\pi}{N+1}\right)\\ \sin\left(\frac{2\mu\pi}{N+1}\right)\\ \vdots\\ \sin\left(\frac{N\mu\pi}{N+1}\right)\end{pmatrix}\otimes\boldsymbol{v}_l, \qquad \begin{matrix}1\leqslant\mu\leqslant N,\\ l=\pm1\end{matrix}, \tag{C11}$$

where Z is the normalization constant $Z=\sqrt{2/(N+1)}$ and $\boldsymbol{v}_l$ is a two-component vector. The eigenstates are degenerate in components of $\boldsymbol{v}_l$; hence, we can choose two orthogonal vectors $\boldsymbol{v}_\alpha$ and $\boldsymbol{v}_\beta$ to get an orthogonal degenerate eigenstates. The energies of the eigenstates $|\psi^0_{\mu l}\rangle$ are (independent of l)

$$E^0_{\mu l} = -2t\cos\left(\frac{\pi\mu}{N+1}\right). \tag{C12}$$

Now we choose the Hamiltonian (6) with the perturbation $\hat{H}_1+\hat{H}_N$, parametrized by Eq. (7) (Model 2). Solving the eigenvalue equation to diagonalize matrix elements of $\hat{H}_{\text{pert}}$ leads to eigenvectors of form

$$\boldsymbol{v}_\alpha = \begin{pmatrix}\sin(\theta_T/2)\\ -\cos(\theta_T/2)\end{pmatrix}, \quad \boldsymbol{v}_\beta = \begin{pmatrix}\cos(\theta_T/2)\\ \sin(\theta_T/2)\end{pmatrix}, \tag{C13}$$

which leads to eigenvalues mentioned in main text

$$E^1_{\mu,\alpha/\beta} = 2\epsilon Z^2\sin^2\left(\frac{\mu\pi}{N+1}\right)(\cos/\sin)^2(\theta_T/2). \tag{C14}$$

Hence, the natural eigenstates for the perturbation are two perpendicular "linearly polarized" [47] strands of p orbitals. The first-order corrections to helicity calculated by Eq. (C10) are then readily obtained. The results are presented graphically for HOMO and HOMO−1 in Fig. 13.

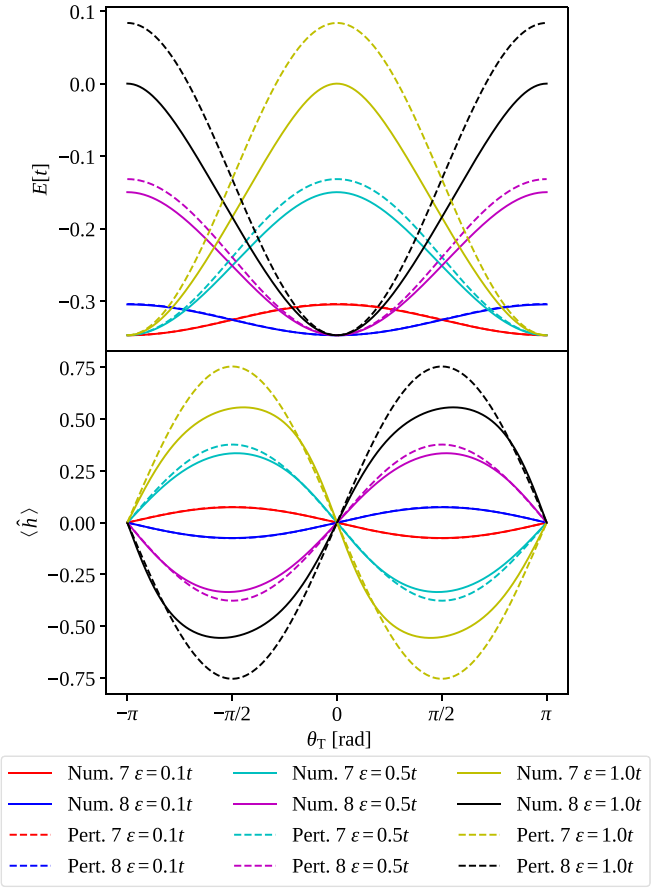

FIG. 13. The energy and helicity $\langle\hat{h}\rangle$ of a doublet of eigenstates, HOMO and HOMO−1, calculated by first-order perturbation theory and numerically by exact diagonalization, for $N=8$. The end-group term with $\epsilon = 0.15t$ and varying twist angle θ_T is added.

APPENDIX D: SUBSTITUTIONAL DISORDER

One way to validate robustness of our results is to investigate presence of onsite substitution in the chain. We model the substitution only in a very simplified way—as a presence of an onsite potential on a single atom in the chain.

We chose the chain of length $N=8$, as in the previous section, with $\epsilon = 0.1t$ and swept through all θ_T while also varying the onsite potential ϵ_4. The Hamiltonian reads

$$\hat{H} \to \hat{H} + \epsilon_4\mathbb{B}_4\otimes\hat{\sigma}_0. \tag{D1}$$

The resulting energy of selected eigenstates and the expectation value of helicality in these eigenstates is presented in Fig. 14. We notice the avoided crossings at 90°. Results for broader choices of ϵ_4 are shown in Fig. 15. Again, the opposite signs of helicality in orbital pairs is observed.

APPENDIX E: EFFECT OF MOLECULAR VIBRATIONS

The Onsager relations derived in this work rely on time-reversal invariance and SL symmetry. Coupling of electrons

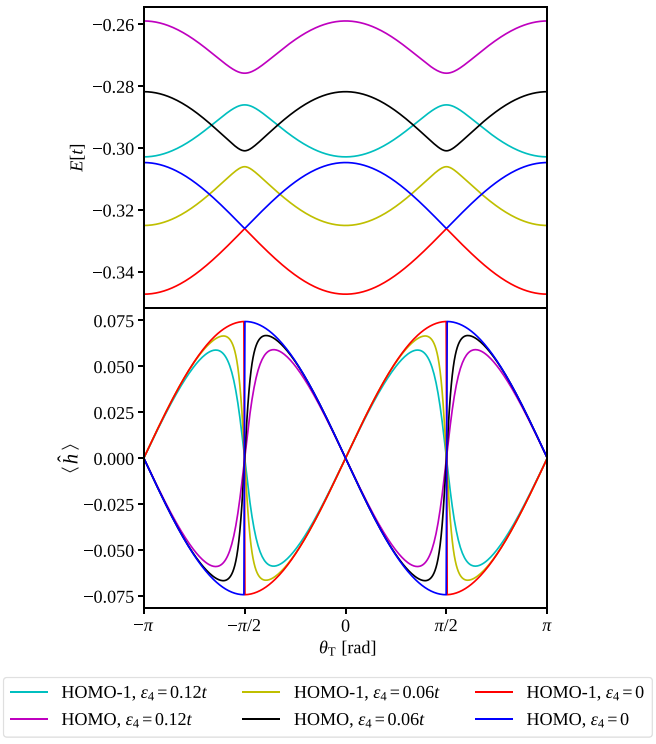

FIG. 14. The energy (top) and the expectation value of helicality (bottom) for several values of the onsite potential. Compared to the ordered case ($\epsilon_4 = 0$), the gap between the eigenstates opens in place of the crossings. The helicality of the pair of states retains opposite sign at any chosen angle θ_T. Here, number of sites $N = 8$ and $\epsilon = 0.1t$.

to molecular vibrations preserves the former but the fate of the latter is discussed here briefly.

To investigate the effects of electron-vibrational coupling, we reformulate the Hamiltonian from first to second quantization, namely,

$$\hat{\mathscr{H}} = \sum_{I,I'} H_{II'} \hat{c}_I^\dagger \hat{c}_{I'},$$

where $\hat{c}_I^\dagger$ and $\hat{c}_I$ denote fermionic creation and annihilation operator; the single-particle basis is indexed by $|I\rangle \equiv |\alpha n\rangle$ [see Eq. (4)], and $H_{II'} = \langle I|\hat{H}|I'\rangle$. The SL symmetry is a condition expressed on the "first-quantized" matrices as $\sum_I (H_{I'I} P_{II''} + H_{II''} P_{I'I}) = 0$ with $P_{II'} = \langle I|\hat{P}|I'\rangle$ as given in Eq. (49) [alternatively Eq. (57)]. The Hamiltonian that describes molecular vibrations, the electronic system and their linearized mutual coupling takes generally the form

$$\hat{\mathscr{K}} = \hat{\mathscr{H}} + \hat{\mathscr{H}}_{\text{vib}}(\hat{b}\,,\,\hat{b}^\dagger) + \sum_{II'} M^v_{II'} \hat{c}_I^\dagger \hat{c}_{I'} (\hat{b}_v + \hat{b}_v^\dagger), \quad \text{(E1)}$$

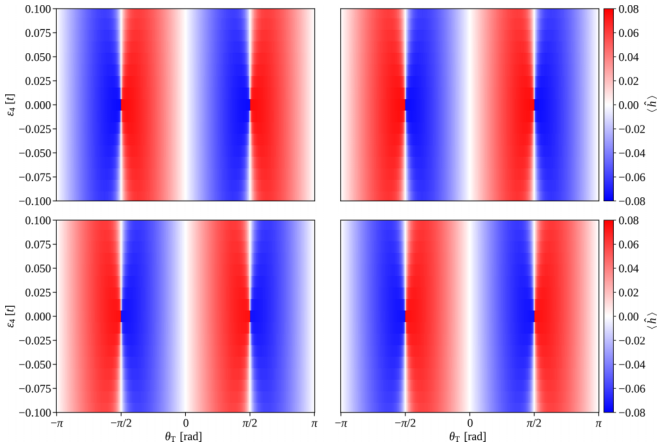

FIG. 15. The expectation value of helicality for HOMO−1, HOMO (bottom row) and LUMO+1, LUMO in a chain of length $N = 8$ with $\epsilon = 0.1t$. We observe that the opposite sign of helicality between the orbital pairs is present.

where $\hat{b}_v^\dagger$ and $\hat{b}_v$ denote bosonic creation and annihilation operators. The electron-vibrational coupling preserves SL symmetry when the coupling elements obey

$$\sum_I \left(M^v_{I'I} P_{II''} + M^v_{II''} P_{I'I} \right) = 0, \quad \text{(E2)}$$

i.e., when the corresponding matrices anticommute. The deviation from the above rule occurs, e.g., when the vibration induces a strong inhomogeneity implying that M^v_{II} is different for different sites.

The interaction of electrons and vibrations in polyynes (infinitely long carbon wires with alternating single and triple bonds) was investigated by Rice *et al.* [70]. The authors used a Su-Schrieffer-Heeger [71] (SSH) model with two electronic bands, p_x and p_y, and a coupling to longitudinal vibrations incorporated as a modulation of the nearest-neighbor hopping elements. The interaction with transverse vibrations is often considered much weaker, as transverse vibrations have a smaller impact on the effective electrostatic potential [72]. Crucially, the modulation of nearest-neighbor hopping amplitudes satisfies condition (E2). An analogous situation occurs in graphene, where the dominant electron-vibrational coupling was assumed to be SL preserving [73,74]. We conclude that SL symmetry will be preserved in vibrating chains as long as the SSH description is valid, even if the lattice deformation is large and the coupling is strong. In this regime, the Onsager relations are expected to hold since the underlying microscopic symmetries are preserved.

[1] J. F. Stoddart, Mechanically interlocked molecules (MIMs)-molecular shuttles, switches, and machines, Angew. Chem. Int. Ed. **56**, 11094 (2017).

[2] C. Cheng and J. F. Stoddart, Wholly synthetic molecular machines, ChemPhysChem **17**, 1780 (2016).

[3] V. Balzani, A. Credi, F. M. Raymo, and J. F. Stoddart, Artificial molecular machines, Angew. Chem. Int. Ed. **39**, 3348 (2000).

[4] S. Kassem, T. van Leeuwen, A. S. Lubbe, M. R. Wilson, B. L. Feringa, and D. A. Leigh, Artificial molecular motors, Chem. Soc. Rev. **46**, 2592 (2017).

[5] F. Jülicher, A. Ajdari, and J. Prost, Modeling molecular motors, Rev. Mod. Phys. **69**, 1269 (1997).

[6] P. Hänggi and F. Marchesoni, Artificial Brownian motors: Controlling transport on the nanoscale, Rev. Mod. Phys. **81**, 387 (2009).

[7] G. J. Simpson, V. García-López, A. D. Boese, J. M. Tour, and L. Grill, How to control singlemolecule rotation, Nat. Commun. **10**, 4631 (2019).

[8] J. Ren, M. Freitag, C. Schwermann, A. Bakker, S. Amirjalayer, A. Rühling, H.-Y. Gao, N. L. Doltsinis, F. Glorius, and H. Fuchs, A unidirectional surface-anchored N-heterocyclic carbene rotor, Nano Lett. **20**, 5922 (2020).

[9] T. Jasper-Toennies, M. Gruber, S. Johannsen, T. Frederiksen, A. Garcia-Lekue, T. Jäkel, F. Roehricht, R. Herges, and R. Berndt, Rotation of ethoxy and ethyl moieties on a molecular platform on Au (111), ACS Nano **14**, 3907 (2020).

[10] S. Stolz, O. Gröning, J. Prinz, H. Brune, and R. Widmer, Molecular motor crossing the frontier of classical to quantum tunneling motion, Proc. Natl. Acad. Sci. USA **117**, 14838 (2020).

[11] F. Eisenhut, T. Kühne, J. Monsalve, S. Srivastava, D. A. Ryndyk, G. Cuniberti, O. Aiboudi, F. Lissel, V. Zobač, R. Robles, N. Lorente, C. Joachim, and F. Moresco, One-way rotation of a chemically anchored single moleculerotor, Nanoscale **13**, 16077 (2021).

[12] M. Schied, D. Prezzi, D. Liu, S. Kowarik, P. A. Jacobson, S. Corni, J. M. Tour, and L. Grill, Chirality-specific unidirectional rotation of molecular motors on Cu(111), ACS Nano **17**, 3958 (2023).

[13] K. H. Au-Yeung, S. Sarkar, T. Kühne, O. Aiboudi, D. A. Ryndyk, R. Robles, F. Lissel, N. Lorente, C. Joachim, and F. Moresco, Thermal with electronic excitation for the unidirectional rotation of a molecule on a surface, J. Phys. Chem. C **127**, 16989 (2023).

[14] G. Srivastava, P. Štacko, J. I. Mendieta-Moreno, S. Edalatmanesh, J. C. M. Kistemaker, G. H. Heideman, L. Zoppi, M. Parschau, B. L. Feringa, and K.-H. Ernst, Driving a third generation molecular motor with electrons across a surface, ACS Nano **17**, 3931 (2023).

[15] Y. Zhang, H. Kersell, R. Stefak, J. Echeverria, V. Iancu, U. G. E. Perera, Y. Li, A. Deshpande, K.-F. Braun, C. Joachim, G. Rapenne, and S.-W. Hla, Simultaneous and coordinated rotational switching of all molecular rotors in a network, Nat. Nanotechnol. **11**, 706 (2016).

[16] K. H. Au-Yeung, S. Sarkar, T. Kühne, O. Aiboudi, D. A. Ryndyk, R. Robles, N. Lorente, F. Lissel, C. Joachim, and F. Moresco, A nanocar and rotor in one molecule, ACS Nano **17**, 3128 (2023).

[17] C. Li, Y. Lu, R. Li, L. Wang, A. Weismann, and R. Berndt, Mechanically interlocked molecular rotors on Pb(100), Nano Lett. **25**, 1504 (2025).

[18] J. A. Skolaut, Molecular motor based on single, chiral, tripodal molecules studied with STM, Ph.D. thesis, Karlsruhe Institute of Technology, 2022.

[19] J. Skolaut, Š. Marek, N. Balzer, M. Camarasa-Gómez, J. Wilhelm, J. Lukášek, M. Valášek, L. Gerhard, F. Evers, M. Mayor, W. Wulfhekel, and R. Korytár, An electrical molecular motor driven by angular momentum transfer, arXiv:2503.05351.

[20] N. Lorente and C. Joachim, Rotations of adsorbed molecules induced by tunneling electrons, in *Building and Probing Small for Mechanics* (Springer, Cham, 2020), pp. 181–194.

[21] F. D. Ribetto, S. E. Deghi, H. L. Calvo, and R. A. Bustos-Marún, A dynamical model for Brownian molecular motors driven by inelastic electron tunneling, J. Chem. Phys. **157**, 164102 (2022).

[22] J.-T. Lü, M. Brandbyge, P. Hedegård, T. N. Todorov, and D. Dundas, Current-induced atomic dynamics, instabilities, and raman signals: Quasiclassical langevin equation approach, Phys. Rev. B **85**, 245444 (2012).

[23] R. Bustos-Marún, G. Refael, and F. von Oppen, Adiabatic quantum motors, Phys. Rev. Lett. **111**, 060802 (2013).

[24] M. Hopjan, G. Stefanucci, E. Perfetto, and C. Verdozzi, Molecular junctions and molecular motors: Including Coulomb repulsion in electronic friction using nonequilibrium Green's functions, Phys. Rev. B **98**, 041405(R) (2018).

[25] R. Korytár and F. Evers, Current-induced mechanical torque in chiral molecular rotors, Beilstein J. Nanotechnol. **14**, 711 (2023).

[26] C. H. Hendon, D. Tiana, A. T. Murray, D. R. Carbery, and A. Walsh, Helical frontier orbitals of conjugated linear molecules, Chem. Sci. **4**, 4278 (2013).

[27] M. H. Garner, A. Jensen, L. O. H. Hyllested, and G. C. Solomon, Helical orbitals and circular currents in linear carbon wires, Chem. Sci. **10**, 4598 (2019).

[28] J. Kohanoff, *Electronic Structure Calculations for Solids and Molecules: Theory and Computational Methods* (Cambridge University Press, Cambridge, 2006).

[29] M. H. Garner, R. Hoffmann, S. Rettrup, and G. C. Solomon, Coarctate and Möbius: The helical orbitals of allene and other cumulenes, ACS Cent. Sci. **4**, 688 (2018).

[30] W. Bro-Jørgensen, M. H. Garner, and G. C. Solomon, Quantification of the helicality of helical molecular orbitals, J. Phys. Chem. A **125**, 8107 (2021).

[31] M. König, H. Buhmann, L. W. Molenkamp, T. Hughes, C.-X. Liu, X.-L. Qi, and S.-C. Zhang, The quantum spin Hall effect: Theory and experiment, J. Phys. Soc. Jpn. **77**, 031007 (2008).

[32] N. P. Armitage, E. J. Mele, and A. Vishwanath, Weyl and Dirac semimetals in three-dimensional solids, Rev. Mod. Phys. **90**, 015001 (2018).

[33] Y. Liu, J. Xiao, J. Koo, and B. Yan, Chirality-driven topological electronic structure of DNA-like materials, Nat. Mater. **20**, 638 (2021).

[34] R. Korytár, J. M. van Ruitenbeek, and F. Evers, Spin conductances and magnetization production in chiral molecular junctions, J. Chem. Phys. **161**, 094111 (2024).

[35] M. Z. Hasan, G. Chang, I. Belopolski, G. Bian, S.-Y. Xu, and J.-X. Yin, Weyl, Dirac and high-fold chiral fermions in topological quantum matter, Nat. Rev. Mater. **6**, 784 (2021).

[36] B. Yan, Structural chirality and electronic chirality in quantum materials, Annu. Rev. Mater. Res. **54**, 97 (2024).

[37] A. H. C. Neto, F. Guinea, N. M. R. Peres, K. S. Novoselov, and A. K. Geim, The electronic properties of graphene, Rev. Mod. Phys. **81**, 109 (2009).

[38] M. I. Katsnelson, *The Physics of Graphene*, 2nd ed. (Cambridge University Press, Cambridge, 2020).

[39] F. Evers, R. Korytár, S. Tewari, and J. M. van Ruitenbeek, Advances and challenges in single-molecule electron transport, Rev. Mod. Phys. **92**, 035001 (2020).

[40] Y. Tsuji, E. Estrada, R. Movassagh, and R. Hoffmann, Quantum interference, graphs, walks, and polynomials, Chem. Rev. **118**, 4887 (2018).

[41] C. A. Coulson and G. S. Rushbrooke, Note on the method of molecular orbitals, Math. Proc. Cambridge Philos. Soc. **36**, 193 (1940).

[42] R. B. Mallion and D. H. Rouvray, The golden jubilee of the Coulson-Rushbrooke pairing theorem, J. Math. Chem. **5**, 1 (1990).

[43] A. Altland and M. R. Zirnbauer, Nonstandard symmetry classes in mesoscopic normal-superconducting hybrid structures, Phys. Rev. B **55**, 1142 (1997).

[44] J. Koutecký, Contribution to the theory of alternant systems, J. Chem. Phys. **44**, 3702 (1966).

[45] F. Schwabl, *Advanced Quantum Mechanics*, 4th ed. (Springer, Heidelberg, 2008), Chap. 11.6.

[46] In the Dirac equation, the term chiral refers to spin-momentum locking.

[47] S. Gunasekaran and L. Venkataraman, Tight-binding analysis of helical states in carbyne, J. Chem. Phys. **153**, 124304 (2020).

[48] A. Arnold, F. Weigend, and F. Evers, Quantum chemistry calculations for molecules coupled to reservoirs: Formalism, implementation, and application to benzenedithiol, J. Chem. Phys. **126**, 174101 (2007).

[49] A. Donarini and M. Grifoni, *Quantum Transport in Interacting Nanojunctions* (Springer, Cham, 2024).

[50] L. P. Kadanoff, *Quantum Statistical Mechanics* (CRC Press, Boca Raton, 2018).

[51] S. S. Schweber, *An Introduction to Relativistic Quantum Field Theory* (Courier Corporation, Mineola, 2005).

[52] C.-K. Chiu, J. C. Y. Teo, A. P. Schnyder, and S. Ryu, Classification of topological quantum matter with symmetries, Rev. Mod. Phys. **88**, 035005 (2016).

[53] The requirement of $\lim_{\epsilon\to\infty} \epsilon\langle x_1|\psi\rangle = 0$ is made here. It is guaranteed by the exponential decay of ψ in the tunnel region.

[54] F. Evers and A. D. Mirlin, Anderson transitions, Rev. Mod. Phys. **80**, 1355 (2008).

[55] L. Onsager, Reciprocal relations in irreversible processes. I., Phys. Rev. **37**, 405 (1931).

[56] L. Onsager, Reciprocal relations in irreversible processes. II., Phys. Rev. **38**, 2265 (1931).

[57] P. Jacquod, R. S. Whitney, J. Meair, and M. Büttiker, Onsager relations in coupled electric, thermoelectric, and spin transport: The tenfold way, Phys. Rev. B **86**, 155118 (2012).

[58] K. Momma and F. Izumi, *VESTA 3* for three-dimensional visualization of crystal, volumetric and morphology data, J. Appl. Crystallogr. **44**, 1272 (2011).

[59] Š. Marek, Electronic structure effects in molecular junctions, Ph.D. thesis, Univerzita Karlova, Matematicko-fyzikální fakulta, 2024.

[60] S. Marek and R. Korytár, Helical orbitals in electrical unidirectional molecular motors [Data set], Zenodo (2025), doi:https://doi.org/10.5281/zenodo.17360146.

[61] N. Bode, S. V. Kusminskiy, R. Egger, and F. von Oppen, Scattering theory of current-induced forces in mesoscopic systems, Phys. Rev. Lett. **107**, 036804 (2011).

[62] F. Elste, G. Weick, C. Timm, and F. von Oppen, Current-induced conformational switching in single-molecule junctions, Appl. Phys. A **93**, 345 (2008).

[63] F. S. Guttesen, Chiral molecular motors, Ph.D. thesis, University of Copenhagen, 2025.

[64] J.-T. Lü, R. B. Christensen, J.-S. Wang, P. Hedegård, and M. Brandbyge, Current-induced forces and hot spots in biased nanojunctions, Phys. Rev. Lett. **114**, 096801 (2015).

[65] R. Gleiter and D. B. Werz, Alkynes between main group elements: From dumbbells via rods to squares and tubes, Chem. Rev. **110**, 4447 (2010).

[66] J. M. van Ruitenbeek, R. Korytár, and F. Evers, Chirality-controlled spin scattering through quantum interference, J. Chem. Phys. **159**, 024710 (2023).

[67] M. Walz, A. Bagrets, and F. Evers, Local current density calculations for molecular films from *ab-initio*, J. Chem. Theory Comput. **11**, 5161 (2015).

[68] P. W. Atkins and R. S. Friedman, *Molecular Quantum Mechanics* (Oxford University Press, Oxford, 2011).

[69] L. D. Landau and E. M. Lifshitz, *Quantum Mechanics: NonRelativistic Theory* (Elsevier, Oxford, 2013), Vol. 3.

[70] M. J. Rice, S. R. Phillpot, A. R. Bishop, and D. K. Campbell, Solitons, polarons, and phonons in the infinite polyyne chain, Phys. Rev. B **34**, 4139 (1986).

[71] A. J. Heeger, S. Kivelson, J. R. Schrieffer, and W.-P. Su, Solitons in conducting polymers, Rev. Mod. Phys. **60**, 781 (1988).

[72] C. Kittel, *Quantum Theory of Solids* (Wiley, New York, 1963)

[73] T. Ando, Physics of graphene: Zero-mode anomalies and roles of symmetry, Prog. Theor. Phys. Suppl. **176**, 203 (2008).

[74] E. Mariani and F. von Oppen, Flexural phonons in freestanding graphene, Phys. Rev. Lett. **100**, 076801 (2008).